The invariant constrained equilibrium edge preimage curve method for the dimension reduction of chemical kinetics

Zhuyin Ren[a] and Stephen B. Pope
Sibley School of Mechanical and Aerospace Engineering, Cornell University, Ithaca, New York 14853

Alexander Vladimirsky and John M. Guckenheimer
Department of Mathematics, Cornell University, Ithaca, New York 14853

(Received 14 October 2005; accepted 24 January 2006; published online 20 March 2006)

This work addresses the construction and use of low-dimensional invariant manifolds to simplify complex chemical kinetics. Typically, chemical kinetic systems have a wide range of time scales. As a consequence, reaction trajectories rapidly approach a hierarchy of attracting manifolds of decreasing dimension in the full composition space. In previous research, several different methods have been proposed to identify these low-dimensional attracting manifolds. Here we propose a new method based on an invariant constrained equilibrium edge (ICE) manifold. This manifold (of dimension n_r) is generated by the reaction trajectories emanating from its (n_r-1)-dimensional edge, on which the composition is in a constrained equilibrium state. A reasonable choice of the n_r represented variables (e.g., n_r "major" species) ensures that there exists a unique point on the ICE manifold corresponding to each realizable value of the represented variables. The process of identifying this point is referred to as species reconstruction. A second contribution of this work is a local method of *species reconstruction*, called ICE-PIC, which is based on the ICE manifold and uses preimage curves (PICs). The ICE-PIC method is *local* in the sense that species reconstruction can be performed without generating the whole of the manifold (or a significant portion thereof). The ICE-PIC method is the first approach that locally determines points on a low-dimensional invariant manifold, and its application to high-dimensional chemical systems is straightforward. The "inputs" to the method are the detailed kinetic mechanism and the chosen reduced representation (e.g., some major species). The ICE-PIC method is illustrated and demonstrated using an idealized H_2/O system with six chemical species. It is then tested and compared to three other dimension-reduction methods for the test case of a one-dimensional premixed laminar flame of stoichiometric hydrogen/air, which is described by a detailed mechanism containing nine species and 21 reactions. It is shown that the error incurred by the ICE-PIC method with four represented species is small across the whole flame, even in the low temperature region. © *2006 American Institute of Physics*. [DOI: 10.1063/1.2177243]

I. INTRODUCTION

It is currently feasible to perform computer simulations of turbulent reactive flows involving order 50 chemical species.[1] For the methodology used in this example, the computational work scales approximately as the square of the number of species; and so, an order of magnitude reduction in cost would result if the chemistry could be adequately described by 16 species instead of 50. Conversely, a chemical mechanism involving 1000 species would increase the cost (compared to the currently feasible 50 species) by a factor of 400, and hence will remain impracticable for some time to come. Chemical mechanisms involving 1000 species or more are not uncommon in the description of the combustion of real fuels. For example, the detailed kinetic mechanism for the primary reference fuel[2] contains 1034 species, which participate in 4236 elementary reactions.

These considerations motivate the well-recognized need for methodologies that radically decrease the computational burden imposed by the direct use of detailed chemical kinetics in reactive flow calculations.

Of the several different types of such methodologies, three approaches that are currently particularly fruitful (and which can be used in combination) are the extraction of skeletal mechanisms from large detailed mechanisms by the elimination of inconsequential species and reactions;[3,4] dimension-reduction techniques, which are reviewed in Refs. 5–7 and are the subject of the current paper; and storage/retrieval methodologies such as *in situ* adaptive tabulation (ISAT),[8] which substantially reduce the number of chemical kinetic computations required in a reactive flow calculation.

The oldest and most commonly used dimension-reduction methodology is based on the quasi-steady-state assumption (QSSA).[9,10] It is useful to outline this method as a means of introducing more general concepts. In the QSSA approach, the n_s chemical species are divided in n_r "major species" (or represented variables) and $n_u=n_s-n_r$ "minor species" (or unrepresented variables). For each of the minor species QSSA is invoked, i.e., the net production rate of the

[a]Author to whom correspondence should be addressed. Fax: (607) 255-1222. Electronic mail: zr26@cornell.edu

minor species by chemical reactions is taken to be zero. The use of QSSA changes the mathematical nature of the model for the chemically reactive system, from one governed by a set of n_s ordinary differential equations (ODEs) to a differential-algebraic system consisting of n_r ODEs and n_u algebraic equations.

In the n_s-dimensional species or composition space, these n_u algebraic equations define an n_r-dimensional manifold, composed of all compositions which satisfy QSSA for the minor species. All compositions which occur in the reactive flow are assumed to lie on (or close to) this manifold, based on the following observation. In a typical combustion process, there is a wide range of time scales present in the chemical mechanism; the very fast time scales are usually associated with local equilibrium or quasisteady states, while the long-term dynamics of the reactive flow are determined by a small number n_r of slow processes.[11–14] Hence, a dimension reduction is achieved: the reactive system can be described on this n_r-dimensional QSSA manifold rather than in the n_s-dimensional full space.

Many other dimension reductions have been proposed, all of which either explicitly or implicitly define a low-dimensional manifold in the full composition space. In addition to QSSA,[9,10,15,16] such methods include rate-controlled constrained equilibrium (RCCE),[17–19] intrinsic low-dimensional manifolds (ILDMs),[20] trajectory-generated low-dimensional manifolds (TGLDMs),[21] flamelet generated manifolds (FGMs),[22] the Roussel-Fraser (RF) algorithm,[23] the method of invariant manifolds,[24] the preimage curve method,[25] and some variants of the above methods.[26–28] While each of the existing approaches can claim some success, and several have been extensively applied, all have either some mathematical shortcomings or difficulties in implementation, especially in higher dimensions.

Among the desirable mathematical properties of low-dimensional manifolds to describe the chemical kinetic system are invariance, continuity, and smoothness. By definition, a manifold is invariant if a composition initially on the manifold remains on the manifold as the composition evolves according to the detailed chemical kinetics. Or, put another way, a manifold is invariant if it is composed of *reaction trajectories* of the full system. Approaches such as RF and TGLDM are invariant, whereas QSSA, RCCE, ILDM, and FGM are not.

The manifold introduced in this work draws on ideas from TGLDM and RCCE, and is called the invariant constrained equilibrium edge (ICE) manifold. As in TGLDM, the n_r-dimensional manifold is generated by the reaction trajectories emanating from an (n_r-1)-dimensional "edge" manifold. As in RCCE, the edge manifold is composed of compositions in constrained chemical equilibrium. By construction, the ICE manifold is invariant, continuous, and piecewise smooth. (As is usual in the chemistry-reduction literature we use the term "manifold" somewhat loosely, where the object described may be only piecewise smooth, whereas the stricter mathematical definition of a manifold requires global smoothness.)

Another desirable property is that the n_r-dimensional manifold be simply parametrized by n_r represented variables. For the given represented variables, we say that a manifold is "not folded" if the compositions on the manifold are given by a graph of a function of the represented variables. In this case, to each realizable value of the represented variables there exists a unique corresponding point on the manifold. Conversely, if a manifold is folded, then there are multiple manifold points corresponding to some values of the represented variables. In our experience it is not difficult to find a set of represented variables such that the ICE manifold is not folded.

For a manifold that is not folded, the process of determining the full composition (on the manifold) from the reduced representation is termed "species reconstruction."[25] An important distinction between dimension-reduction methodologies is whether or not they are *local*. By definition, in local methods, species reconstruction can be performed (for given values of the represented variables) without constructing the whole (or a significant portion) of the manifold. Approaches such as QSSA, RCCE, and ILDM are local, and in these cases species reconstruction involves, respectively, the solution of the nonlinear QSSA equations to determine the mass fractions of the minor species, a constrained equilibrium calculation, and a Newton iteration to determine the corresponding ILDM point. In contrast, methods such as TGLDM, FGM, and RF are *global*—they require the generation of the entire manifold. The computational implementation of such global methods soon becomes impracticable as the dimensionality of the manifold increases.

A second contribution of the present work is the development of a local method to perform species reconstruction based on the ICE manifold. The method is based on preimage curves (PIC),[25] and consequently is called the ICE-PIC method. Given the values of the represented variables, the ICE-PIC method performs species reconstruction through three steps which are as follows: first, the determination of the constrained equilibrium composition; second, in the full composition space, following the *constrained equilibrium preimage curve* (CE-PIC) to a particular point on the edge of the manifold; and, third, following the reaction trajectory from this point along the ICE manifold to the required point—the reconstructed composition.

We note that this ICE-PIC method is currently the only dimension-reduction methodology that is both based on an invariant manifold, and for which there is a local method of species reconstruction.

Compared to other local methods (QSSA, RCCE, ILDM), the ICE-PIC method is computationally more expensive. As discussed by Ren and Pope,[25] if a dimension-reduction technique is used in combination with a storage/retrieval methodology (e.g., ISAT), then (within reason) the cost of species reconstruction is not of primary concern. This is because, in a typical application, the overall computational cost is dominated by retrievals, whereas species reconstruction needs to be performed only in the relatively infrequent storage events.

The outline of the remainder of the paper is as follows. In Sec. II the mathematical formulation is developed for an isobaric, isothermal reacting system, culminating in the definition of the ICE manifold and an examination of its prop-

erties. The development is largely geometrical, involving various curves and manifolds and their intersections. We illustrate the geometrical constructions involved for an idealized H_2/O system, contrived to yield two-dimensional manifolds in three-dimensional space, so that they can be depicted in figures. In Sec. III the ICE-PIC method is described. The extension of the ICE manifold and the ICE-PIC method from isothermal systems to adiabatic systems is discussed in Sec. IV. In Sec. V we compare the performance of different species reconstruction methodologies (ICE-PIC, RCCE, ILDM, QSSA) for the test case of a premixed laminar hydrogen/air flame described by the nine-species detailed mechanism of Li *et al.*[29] In Sec. VI we conclude by summarizing the properties of our approach and describing the directions of future work.

II. THE INVARIANT CONSTRAINED EQUILIBRIUM EDGE (ICE) MANIFOLD

In this section we develop the sequence of concepts and notation needed to define the ICE manifold. In Sec. II B, we introduce the idealized H_2/O system as a specific example designed to illustrate the various geometric objects involved.

A. Homogeneous reacting system

We consider a closed, homogeneous, isobaric reacting system. To present and illustrate the new ideas, we consider an isothermal system. The extension to an adiabatic system is discussed in Sec. IV, and the method is applied to an adiabatic system in the tests shown in Sec. V.

The system consists of n_s chemical species, composed on n_e elements. The elemental composition of the species is given by the $n_s \times n_e$ elemental matrix $\mathbf{E}$: the component E_{ij} indicates the number of atoms of element j in a molecule of species i. The molecular weights of the species are given by $\mathbf{W}=\{W_1, W_2, \ldots, W_{n_s}\}$. Different n_s-vectors can be used to represent the composition of the system at any time, e.g., the moles of the species $\mathbf{N}$, their mass fractions $\mathbf{Y}$, or their specific moles $\mathbf{z}$ $(z_i=Y_i/W_i)$. We use the specific moles $\mathbf{z}=\{z_1, z_2, \ldots, z_{n_s}\}$.

In this work we take a geometric view and use the notation of linear vector spaces. The specific moles $\mathbf{z}$ is a vector in the *full composition space* $\mathcal{C}$, which is defined to be a real n_s-dimensional Euclidean space with canonical basis vectors $\mathbf{e}_i$, $i=1,2,\ldots,n_s$. Similarly $\mathbf{W}$ and the columns of $\mathbf{E}$ are vectors in related n_s-dimensional spaces. The specific moles satisfy a normalization condition which can be written

$$\sum_{i=1}^{n_s} z_i W_i = \mathbf{z}^T \mathbf{W} = 1. \tag{1}$$

This is equivalent to the mass fractions summing to unity.

During chemical reactions, atoms are rearranged into different molecules, but of course the number of atoms of each element is conserved (since the system considered is closed). The specific moles of atoms of element i is denoted by z_i^e and the n_e vector of element specific moles is given by

TABLE I. Chemical mechanism of the ideal H_2/O system. A in mol/cm/s/K; E_a in cal/mole; $k^+=AT^\beta \exp(-E_a/\mathcal{R}T)$; $\mathcal{R}$ universal gas constant. M represents a third body that could be any of the species H, H_2, OH, O, H_2O, and N_2. The collision efficiencies for the third bodies are $f_H=1$, $f_{H_2}=2.5$, $f_{OH}=1$, $f_O=1$, $f_{H_2O}=12$, and $f_{N_2}=1$.

	A	β	E_a
(R1) $O+H_2 \Leftrightarrow H+OH$	5.08×10^4	2.7	6290.0
(R2) $H_2+OH \Leftrightarrow H_2O+H$	2.16×10^8	1.5	3430.0
(R3) $O+H_2O \Leftrightarrow OH+OH$	2.97×10^6	2.0	13 400.0
(R4) $H_2+M \Leftrightarrow H+H+M$	4.58×10^{19}	−1.4	104 380.0
(R5) $O+H+M \Leftrightarrow OH+M$	4.71×10^{18}	−1.0	0.0
(R6) $H+OH+M \Leftrightarrow H_2O+M$	3.80×10^{22}	−2.0	0.0

$$\mathbf{z}^e = \mathbf{E}^T \mathbf{z}. \tag{2}$$

Thus for the system considered in Secs. II and III, conserved quantities (fixed for all time) are the mass m, the pressure p, the temperature T, and the element specific moles $\mathbf{z}^e$. (Note that $\mathbf{z}^e$ satisfies the normalization condition $\mathbf{a}^T\mathbf{z}^e=1$, where $\mathbf{a}=\{a_1, a_2, \ldots, a_{n_e}\}$ are the atomic weights of the elements, which, in view of the relation $\mathbf{W}=\mathbf{E}\mathbf{a}$, is consistent with Eq. (1).)

Given that the n_e element specific moles $\mathbf{z}^e$ are conserved, the reactive system can be described in the (n_s-n_e)-dimensional *reactive affine space*, defined by

$$\mathcal{C}(\mathbf{z}^e) \equiv \{\mathbf{z} | \mathbf{E}^T\mathbf{z} = \mathbf{z}^e, \mathbf{z} \in \mathcal{C}\}. \tag{3}$$

And the non-negativity of the species confines the compositions to the *realizable region* of this reactive affine space, defined by

$$\mathcal{C}^+(\mathbf{z}^e) \equiv \{\mathbf{z} | z_i \geqslant 0, \mathbf{E}^T\mathbf{z} = \mathbf{z}^e, \mathbf{z} \in \mathcal{C}\}. \tag{4}$$

This is a bounded convex polytope.

B. Idealized H_2/O system

To illustrate the ideas developed here, we consider a specific chemically reactive system. So that we can draw the various geometric objects in three-dimensional space, we choose a system with $n_s-n_e=3$. Specifically, we consider the six species H_2, O, H_2O, H, OH, and N_2, containing the three elements H, O, and N. Compared to the standard representation of H_2/O_2 chemistry, the species O_2, HO_2, and H_2O_2 are absent (as are NO and related species). The system considered is therefore artificial, especially because of the omission of O_2. In Sec. V we present test results based on the full H_2/O_2 system.

In the examples given below, we take $p=1$ atm, $T=3000$ K, and the specific moles of the elements H, O, and N are 0.012 34, 0.004 11, and 0.065 81 kmol/kg, respectively. We use the mechanism of Li *et al.*,[29] stripping out the absent species. The resulting mechanism has six reversible reactions and is given in Table I.

Figure 1 shows the realizable region $\mathcal{C}^+(\mathbf{z}^e)$ for this idealized system. In order to display it in an easily understood space, the three-dimensional region $\mathcal{C}^+(\mathbf{z}^e)$ is shown projected onto the three-dimensional subspace of $\mathcal{C}$, with basis vectors corresponding to the first three species H_2, O, and H_2O. As may be seen, $\mathcal{C}^+(\mathbf{z}^e)$ is a five-sided wedge-shaped

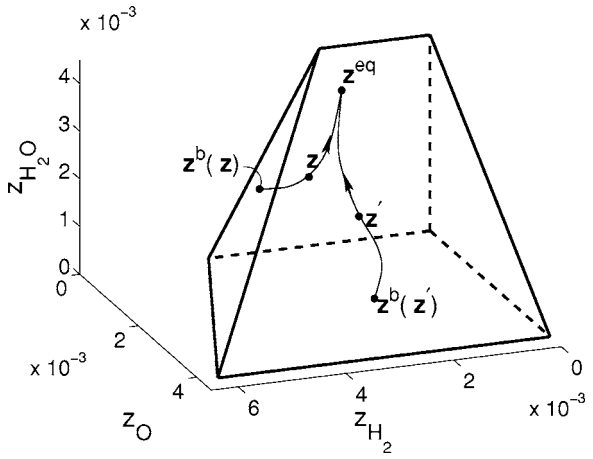

FIG. 1. Sketch, in the H_2-O-H_2O subspace, of the realizable region $\mathcal{C}^+(\mathbf{z}^e)$ for the idealized H_2/O system. Two hypothetical reaction trajectories are sketched, through the points $\mathbf{z}$ and $\mathbf{z}'$, starting from the boundary origin points $\mathbf{z}^b(\mathbf{z})$ and $\mathbf{z}^b(\mathbf{z}')$ and ending at the single equilibrium point $\mathbf{z}^{eq}(\mathbf{z}^e)$.

convex polytope. Its boundary $\partial\mathcal{C}^+(\mathbf{z}^e)$ is made up of five (two-dimensional) facets, on each of which at least one component of $\mathbf{z}$ is zero, whereas in the interior of $\mathcal{C}^+(\mathbf{z}^e)$ all components of $\mathbf{z}$ are strictly positive.

C. Gibbs function, entropy, and chemical equilibrium

All thermodynamic variables—energy, enthalpy, entropy, etc.—are scalar functions defined in $\mathcal{C}^+(\mathbf{z}^e)$. Of particular interest is the Gibbs function $G(\mathbf{z})$. It is well known (see, e.g., Refs. 30 and 31) that $G(\mathbf{z})$ is a strictly convex function with a unique global minimum in the interior of $\mathcal{C}^+(\mathbf{z}^e)$. For the isothermal, isobaric systems under consideration, the location of this minimum corresponds to chemical equilibrium and is denoted by $\mathbf{z}^{eq}(\mathbf{z}^e)$. On a facet of the boundary $\partial\mathcal{C}^+(\mathbf{z}^e)$, the gradient of the Gibbs function ∇G is infinite in magnitude and its direction is that of the outward-pointing normal.[30]

For a system that is adiabatic (as opposed to isothermal) the equilibrium composition is the unique point in the interior of $\mathcal{C}^+(\mathbf{z}^e)$ at which the entropy is maximum.

D. Reaction trajectories

Due to chemical reactions, the composition $\mathbf{z}(t)$ evolves in time t according to the autonomous set of ordinary differential equations (ODEs)

$$\frac{d\mathbf{z}(t)}{dt} = \mathbf{S}(\mathbf{z}(t)), \tag{5}$$

where the rate-of-change vector $\mathbf{S}(\mathbf{z})$ is determined by the detailed chemical kinetic mechanism.

The solutions of Eq. (5) are conveniently denoted by the *reaction mapping* (or flow) $\mathbf{R}(\mathbf{z},t)$, which is defined by

$$\mathbf{R}(\mathbf{z},0) = \mathbf{z}, \quad \frac{\partial\mathbf{R}(\mathbf{z},t)}{\partial t} = \mathbf{S}(\mathbf{R}(\mathbf{z},t)). \tag{6}$$

Thus, $\mathbf{R}(\mathbf{z},t)$ is the solution to Eq. (5) after time t, starting from the initial condition $\mathbf{z}$. As depicted in Fig. 1, for fixed $\mathbf{z}$ and variable t (positive and negative), $\mathbf{R}(\mathbf{z},t)$ represents the *reaction trajectory* through $\mathbf{z}$.

The rate vector $\mathbf{S}$ has the following properties:

(1) $\mathbf{E}^T\mathbf{S}=0$, so that the elemental composition ($\mathbf{E}^T\mathbf{z}=\mathbf{z}^e$) is conserved. As a consequence, the reaction trajectory remains in the (n_s-n_e)-dimensional reactive affine space containing $\mathbf{z}$.

(2) $|\mathbf{S}|>0$ for $\mathbf{z}\neq\mathbf{z}^{eq}(\mathbf{z}^e)$. That is, the mixture is reactive everywhere, except at equilibrium. This is generally the case in the interior of $\mathcal{C}^+(\mathbf{z}^e)$, and we assume that the mechanism is such that it is also the case on the boundary.

(3) $\mathbf{S}^T\nabla G<0$ for $\mathbf{z}\neq\mathbf{z}^{eq}(\mathbf{z}^e)$, where ∇G is the gradient of the Gibbs function, $\nabla G=\{\partial G/\partial z_1, \partial G/\partial z_2, \ldots, \partial G/\partial z_{n_s}\}$. In other words the Gibbs function is a strictly decreasing function of time along a reaction trajectory until the equilibrium composition is attained (in infinite time). This follows from the law of mass action and the second law of thermodynamics.

(4) On the boundary $\partial\mathcal{C}^+(\mathbf{z}^e)$, $\mathbf{S}$ cannot point outward the interior of $\mathcal{C}^+(\mathbf{z}^e)$. This result stems from the law of mass action and it ensures that reaction trajectories originating in $\mathcal{C}^+(\mathbf{z}^e)$ remain realizable. [It also follows from property (3) and from the properties of ∇G on the boundary.]

It follows from these four properties that the reaction trajectory through $\mathbf{z}$ remains in $\mathcal{C}^+(\mathbf{z}^e)$ (for $\mathbf{z}^e=\mathbf{E}^T\mathbf{z}$); at large positive times the trajectory tends to the equilibrium point, i.e., $\mathbf{R}(\mathbf{z},\infty)=\mathbf{z}^{eq}(\mathbf{z}^e)$; and at a finite (but possibly large) negative time, denoted by $-\tau^b(\mathbf{z})$, the trajectory intersects the boundary $\partial\mathcal{C}^+(\mathbf{z}^e)$. Denoting this intersection by $\mathbf{z}^b(\mathbf{z})$, we therefore have

$$\mathbf{R}(\mathbf{z},-\tau^b(\mathbf{z})) = \mathbf{z}^b(\mathbf{z}) \tag{7}$$

and

$$\mathbf{R}(\mathbf{z}^b(\mathbf{z}),\tau^b(\mathbf{z})) = \mathbf{z}. \tag{8}$$

Two different reaction trajectories, through points $\mathbf{z}$ and $\mathbf{z}'$, are shown in Fig. 1. Note that the different trajectories have different *boundary origins*, $\mathbf{z}^b(\mathbf{z})$ and $\mathbf{z}^b(\mathbf{z}')$, but the same ending point, i.e., $\mathbf{z}^{eq}(\mathbf{z}^e)$.

The $n_s\times n_s$ *sensitivity matrix* $\mathbf{A}(\mathbf{z},t)$ is defined to be the derivative of the reaction mapping

$$A_{ij}(\mathbf{z},t) \equiv \frac{\partial R_i(\mathbf{z},t)}{\partial z_j}. \tag{9}$$

This is a very important quantity in the analysis which follows, because it describes the perturbation of the trajectory caused by an infinitesimal perturbation to the initial condition $\mathbf{z}$. Specifically for infinitesimal dt and $d\mathbf{z}$, we have

$$\begin{aligned}\mathbf{R}(\mathbf{z}+d\mathbf{z},t+dt) &= \mathbf{R}(\mathbf{z},t)+\mathbf{A}(\mathbf{z},t)d\mathbf{z}+\mathbf{S}(\mathbf{R}(\mathbf{z},t))dt \\ &= \mathbf{R}(\mathbf{z},t)+\mathbf{A}(\mathbf{z},t)(d\mathbf{z}+\mathbf{S}(\mathbf{z})dt),\end{aligned} \tag{10}$$

where the second step follows from $\mathbf{S}(\mathbf{R}(\mathbf{z},t))=\mathbf{A}(\mathbf{z},t)\mathbf{S}(\mathbf{z})$.[14]

Numerically, Eqs. (5) and (9) for $\mathbf{R}$ and $\mathbf{A}$ are integrated together forward in time using the code DDASAC,[32] with the Jacobian $\mathbf{J}$ ($J_{ij}\equiv\partial S_i/\partial z_j$) being evaluated by automatic differentiation using ADIFOR.[33]

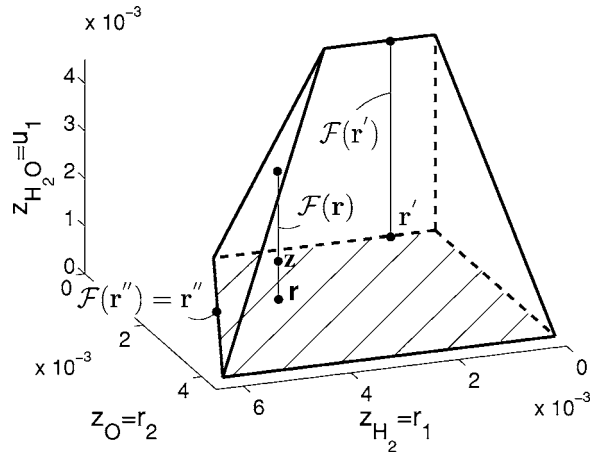

FIG. 2. Sketch, in the active subspace, of the reduced realizable region $\mathcal{B}^+(\mathbf{z}^e)$ (shaded), which is the perpendicular projection of the realizable region $\mathcal{C}^+(\mathbf{z}^e)$ onto the reduced subspace. The reduced composition $\mathbf{r}$ is shown, corresponding to the full composition $\mathbf{z}$. The sketch also shows the one-dimensional feasible regions $\mathcal{F}(\mathbf{r})$ and $\mathcal{F}(\mathbf{r}')$ corresponding to the interior and boundary points $\mathbf{r}$ and $\mathbf{r}'$; and the zero-dimensional feasible region corresponding to the boundary point $\mathbf{r}''$.

E. Reduced composition

The state of the system is completely specified by p, T, and $\mathbf{z}$. The idea of dimension reduction is to approximate the dynamics of the system using fewer variables, which here we take to be p, T, $\mathbf{z}^e$, and the reduced composition $\mathbf{r}$, where $\mathbf{r}=\{r_1,r_2,\ldots,r_{n_r}\}$ is a specified set of n_r *represented variables*, for $1\leqslant n_r<(n_s-n_e)$. Usually, as in the examples below, the reduced compositions are specified as certain major species. But we allow for a more general linear combination of species by defining

$$\mathbf{r}=\mathbf{B}^T\mathbf{z}, \tag{11}$$

where $\mathbf{B}$ is a specified $n_s\times n_r$ matrix (such that $[\mathbf{E}\,\mathbf{B}]$ has independent columns).

For the idealized H_2/O system, we take $n_r=2$ and specify the reduced compositions to be the specific moles of H_2 and O. Thus, with H_2 and O being the first and second species, we have $r_1=z_1$, $r_2=z_2$; and the elements of the matrix $\mathbf{B}$ are zero, except for $B_{11}=B_{22}=1$.

The reduced composition $\mathbf{r}$ is an n_r-vector in the *reduced composition space*

$$\mathcal{B}(\mathbf{z}^e)\equiv\{\mathbf{r}|\mathbf{r}=\mathbf{B}^T\mathbf{z},\mathbf{E}^T\mathbf{z}=\mathbf{z}^e,\mathbf{z}\in\mathcal{C}\}, \tag{12}$$

and it is confined to the *reduced realizable region*

$$\mathcal{B}^+(\mathbf{z}^e)\equiv\{\mathbf{r}|\mathbf{r}=\mathbf{B}^T\mathbf{z},\mathbf{z}\in\mathcal{C}^+(\mathbf{z}^e)\}. \tag{13}$$

In Fig. 2, the horizontal r_1-r_2 plane is the reduced composition space $\mathcal{B}(\mathbf{z}^e)$, and the shaded quadrilateral is the reduced realizable region, $\mathcal{B}^+(\mathbf{z}^e)$. Given the composition $\mathbf{z}$, the reduced composition $\mathbf{r}$ is simply the orthogonal projection onto the r_1-r_2 plane. Note that the interior of $\mathcal{C}^+(\mathbf{z}^e)$ is mapped to the interior of $\mathcal{B}^+(\mathbf{z}^e)$: but the boundary of $\mathcal{C}^+(\mathbf{z}^e)$ is mapped both to the boundary $\partial\mathcal{B}^+(\mathbf{z}^e)$ and to the interior of $\mathcal{B}^+(\mathbf{z}^e)$.

It is convenient to define a set of n_u *unrepresented compositions* $\mathbf{u}$, for $n_u=n_s-n_e-n_r$. In general we specify an $n_s\times n_u$ matrix $\mathbf{U}$ such that $[\mathbf{E}\,\mathbf{B}\,\mathbf{U}]$ spans the composition space $\mathcal{C}$, and then we define

$$\mathbf{u}=\mathbf{U}^T\mathbf{z}. \tag{14}$$

The columns of $[\mathbf{E}\,\mathbf{B}\,\mathbf{U}]$ provide an alternative basis for the composition space $\mathcal{C}$, and $\{\mathbf{z}^e,\mathbf{r},\mathbf{u}\}=\{\mathbf{E}^T\mathbf{z},\mathbf{B}^T\mathbf{z},\mathbf{U}^T\mathbf{z}\}$ contains the same information as $\mathbf{z}$.

For the idealized H_2/O system, we have $n_u=6-3-2=1$, and we specify u_1 to be the specific moles of H_2O. Thus, with H_2O being the third species in the ordering, the components of $\mathbf{U}$ are zero, except for $U_{31}=1$. In Fig. 2, the vertical axis is u_1.

Many spaces and subspaces can be defined in terms of $\mathbf{E}$, $\mathbf{B}$, and $\mathbf{U}$. These include *span*$(\mathbf{E})$, the element subspace; *span*$(\mathbf{E})^\perp$, the reactive subspace [to which $\mathbf{S}(\mathbf{z})$ belongs when nondimensionalized]; *span*$(\mathbf{B})$, the reduced subspace; *span*$([\mathbf{E}\,\mathbf{B}])$, the represented subspace; *span*$(\mathbf{U})$, the unrepresented subspace; and *span*$([\mathbf{B}\,\mathbf{U}])$, the active subspace, which is the subspace in which Fig. 2 is sketched.

F. Attracting manifolds and species reconstruction

From one perspective, dimension reduction consists primarily of identifying an n_r-dimensional attracting manifold $\mathcal{M}(\mathbf{z}^e)$ in the realizable region $\mathcal{C}^+(\mathbf{z}^e)$. For the methods considered in Sec. III, for each point $\mathbf{r}$ in the reduced realizable region $\mathcal{B}^+(\mathbf{z}^e)$, there is a unique corresponding point on the manifold, denoted by $\mathbf{z}^{\mathcal{M}}(\mathbf{z}^e,\mathbf{r})$. That is, the manifold $\mathcal{M}(\mathbf{z}^e)$ is not folded: it is given by a graph of a function of the represented variables, namely, $\mathbf{z}^{\mathcal{M}}(\mathbf{z}^e,\mathbf{r})$. By assumption, the compositions which occur lie close to $\mathcal{M}(\mathbf{z}^e)$, and the dynamics are well approximated by those on $\mathcal{M}(\mathbf{z}^e)$.

A closely related perspective is that of *species reconstruction*,[25] which, given $\mathbf{z}^e$ and $\mathbf{r}$, seeks to determine $\mathbf{z}^{\mathcal{M}}(\mathbf{z}^e,\mathbf{r})$. The distinction between these two perspectives is that in species reconstruction the goal is to determine a single manifold point, without generating or representing the whole manifold (or a significant portion of it).

In species reconstruction, an important concept is that of the *feasible region*. Given the reduced representations $\mathbf{z}^e$ and $\mathbf{r}$, the feasible region $\mathcal{F}(\mathbf{z}^e,\mathbf{r})$ is defined as the union of compositions $\mathbf{z}$ in $\mathcal{C}^+(\mathbf{z}^e)$ which have the reduced composition $\mathbf{r}$, i.e.,

$$\mathcal{F}(\mathbf{z}^e,\mathbf{r})\equiv\{\mathbf{z}|\mathbf{B}^T\mathbf{z}=\mathbf{r},\mathbf{z}\in\mathcal{C}^+(\mathbf{z}^e)\}. \tag{15}$$

Given $\mathbf{z}^e$ and $\mathbf{r}$, without further knowledge or assumptions, it is not generally possible to determine $\mathbf{z}$ uniquely: the unrepresented composition $\mathbf{u}$ is not known. But it is known that $\mathbf{z}$ is in the feasible region $\mathcal{F}(\mathbf{z}^e,\mathbf{r})$. For $\mathbf{r}$ in the interior of $\mathcal{B}^+(\mathbf{z}^e)$, the feasible region is an n_u-dimensional convex polytope. But for $\mathbf{r}$ being on the boundary $\partial\mathcal{B}^+(\mathbf{z}^e)$, the dimensionality can be between n_u and zero.

Figure 2 is a sketch of the feasible region for the idealized H_2/O system (for which $n_u=1$). As shown in the figure, for $\mathbf{r}$ in the interior of $\mathcal{B}^+(\mathbf{z}^e)$, $\mathcal{F}$ is one-dimensional. The feasible regions corresponding to the upper and right boundaries are one-dimensional (parametrized by u_1), whereas those corresponding to the lower and left boundaries are zero-dimensional (given by $u_1=0$).

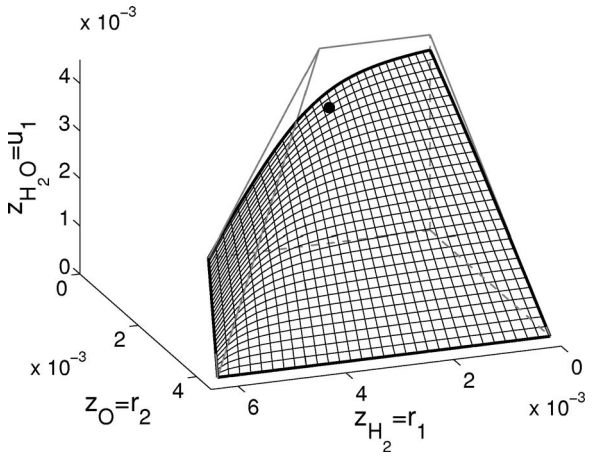

FIG. 3. The computed constrained equilibrium manifold (grid manifold) with H_2 and O being the represented species for the idealized H_2/O system. The dot is the chemical equilibrium composition of the system. The bold curves and lines form the constrained equilibrium edge, which is the intersection between the constrained equilibrium manifold and the boundary of the realizable region.

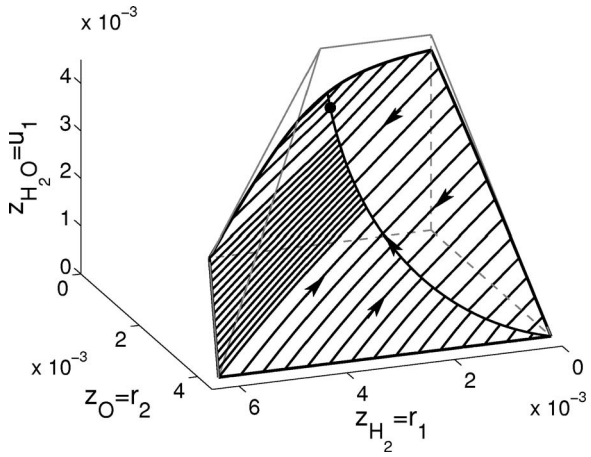

FIG. 4. The invariant constrained-equilibrium edge (ICE) manifold for the idealized system, which is the union of the reaction trajectories from the constrained equilibrium edge (bold lines and curves).

G. Constrained equilibrium manifold

In the rate-controlled constrained equilibrium (RCCE) method developed by Keck and Gillespie,[17,18] the n_r-dimensional attracting manifold is taken to be the *constrained equilibrium manifold* (CEM), which we denote by $\mathcal{M}^{\mathrm{CE}}(\mathbf{z}^e)$. Here we use the CEM for the different purposes.

In the isobaric, isothermal systems being considered, for the given $\mathbf{z}^e$ and $\mathbf{r}$, the corresponding point on the CEM, denoted by $\mathbf{z}^{\mathrm{CE}}(\mathbf{z}^e,\mathbf{r})$, is the point in the feasible region at which the Gibbs function $G(\mathbf{z})$ is minimum. And the CEM is defined as the union of all such points

$$\mathcal{M}^{\mathrm{CE}}(\mathbf{z}^e) \equiv \{\mathbf{z}=\mathbf{z}^{\mathrm{CE}}(\mathbf{z}^e,\mathbf{r})|\mathbf{r} \in \mathcal{B}^+(\mathbf{z}^e)\}. \quad (16)$$

This manifold is known[30] to have ideal mathematical properties in many respects: $\mathbf{z}^{\mathrm{CE}}(\mathbf{z}^e,\mathbf{r})$ exists and is unique for all $\mathbf{r}$ in $\mathcal{B}^+(\mathbf{z}^e)$, $\mathcal{M}^{\mathrm{CE}}(\mathbf{z}^e)$ is smooth, and efficient numerical methods exist to compute $\mathbf{z}^{\mathrm{CE}}$.[31,34–36] These are based on the method of Lagrange multipliers, which in this context are called *constraint potentials*. However, $\mathcal{M}^{\mathrm{CE}}(\mathbf{z}^e)$ is not invariant: reaction trajectories starting on $\mathcal{M}^{\mathrm{CE}}(\mathbf{z}^e)$ can move away from it, although they eventually return because the equilibrium point $\mathbf{z}^{\mathrm{eq}}(\mathbf{z}^e)$ is in $\mathcal{M}^{\mathrm{CE}}(\mathbf{z}^e)$.

The CEM for the idealized H_2/O system is shown in Fig. 3. In this figure the bold line shows the *constrained equilibrium edge* $\partial\mathcal{M}^{\mathrm{CE}}(\mathbf{z}^e)$, defined (in general) as the intersection between $\mathcal{M}^{CE}(\mathbf{z}^e)$ and the boundary of the realizable region

$$\partial\mathcal{M}^{\mathrm{CE}}(\mathbf{z}^e) \equiv \mathcal{M}^{\mathrm{CE}}(\mathbf{z}^e) \cap \partial\mathcal{C}^+(\mathbf{z}^e). \quad (17)$$

Because of the convexity of the Gibbs function, to each point in the boundary $\partial\mathcal{B}^+(\mathbf{z}^e)$ of the reduced realizable region there is a unique corresponding point in the constrained equilibrium edge, which is equivalently given by

$$\partial\mathcal{M}^{\mathrm{CE}}(\mathbf{z}^e) = \{\mathbf{z}=\mathbf{z}^{\mathrm{CE}}(\mathbf{z}^e,\mathbf{r})|\mathbf{r} \in \partial\mathcal{B}^+(\mathbf{z}^e)\}. \quad (18)$$

As discussed in Sec. IV, for adiabatic (as opposed to isothermal) systems, the same concepts apply, but based on the maximization of entropy, rather than on the minimization of the Gibbs function.

H. Invariant constrained equilibrium edge (ICE) manifold

A conceptually simple way to obtain an n_r-dimensional invariant manifold is to define it as the union of the reaction trajectories originating from points in a specified (n_r-1)-dimensional manifold transversal to the vector field $\mathbf{S}(\mathbf{z})$. This is the idea behind the method of trajectory-generated low-dimensional manifolds (TGLDMs) advanced by Pope and Maas[21] and studied by others.[23,26,27] Different n_r-dimensional invariant manifolds can be generated starting from different specifications of (n_r-1)-dimensional manifolds. However, the invariant manifolds converge together at a rate determined by the ratio of the fast and slow time scales in the chemical kinetics. We use the TGLDM method here, taking the (n_r-1)-dimensional constrained equilibrium edge to define the origin of the trajectories.

We now state these ideas more precisely. We denote by $\mathcal{M}^{\mathrm{ICE}}(\mathbf{z}^e)$ the attracting low-dimensional manifold introduced here, and call it the *invariant, constrained equilibrium edge manifold* or the *ICE manifold* for short. It is defined by

$$\mathcal{M}^{\mathrm{ICE}}(\mathbf{z}^e) \equiv \{\mathbf{z}|\mathbf{z}=\mathbf{R}(\mathbf{z}^g,t), t \geqslant 0, \mathbf{z}^g \in \partial\mathcal{M}^{\mathrm{CE}}(\mathbf{z}^e)\}, \quad (19)$$

that is, the ICE manifold is the union of all reaction trajectories $\mathbf{R}(\mathbf{z}^g,t)$ (forward in time) emanating from *generating boundary points* $\mathbf{z}^g$ in the edge of the constrained equilibrium manifold $\partial\mathcal{M}^{\mathrm{CE}}(\mathbf{z}^e)$. Obviously, the ICE manifold contains the equilibrium point $\mathbf{z}^{\mathrm{eq}}(\mathbf{z}^e)$.

The ICE manifold for the idealized H_2/O system is shown in Fig. 4. As may be seen from the figure, from each point in $\partial\mathcal{M}^{\mathrm{CE}}(\mathbf{z}^e)$, the reaction trajectory proceeds (almost as a straight line) to the observed curve, which is a highly attracting one-dimensional manifold. Although not evident from the figure, the trajectories then turn sharply to join this one-dimensional manifold and proceed to the equilibrium point.

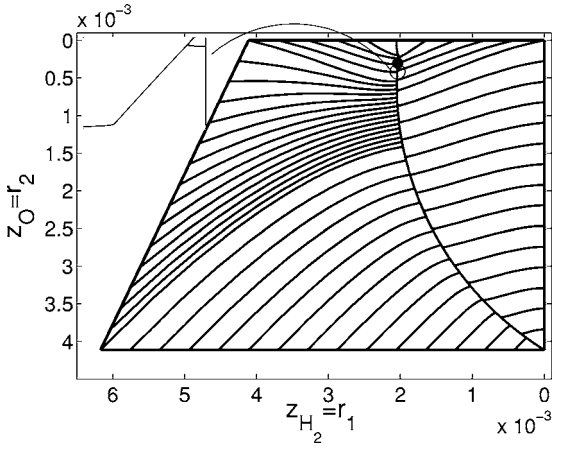

FIG. 5. The projection of the ICE manifold onto the reduced composition space $\mathcal{B}(\mathbf{z}^e)$, shown by the projected trajectories originating on the edge $\partial\mathcal{B}^+(\mathbf{z}^e)$ (bold lines). The fact that the projected trajectories do not cross demonstrates that this ICE manifold is regular: to each point $\mathbf{r}$ in $\mathcal{B}^+(\mathbf{z}^e)$ there is a unique manifold point $\mathbf{z}^{\mathrm{ICE}}(\mathbf{z}^e,\mathbf{r})$. (The directions of the r_1 and r_2 axes are chosen to facilitate comparisons with the previous 3D illustrations.)

Figure 5 shows the projection of the ICE manifold onto the reduced composition space $\mathcal{B}(\mathbf{z}^e)$. Note that to every point $\mathbf{r}$ in the boundary $\partial\mathcal{B}^+(\mathbf{z}^e)$ of the reduced realizable region there is a unique corresponding constrained equilibrium composition $\mathbf{z}^{\mathrm{CE}}(\mathbf{z}^e,\mathbf{r})$, and hence the starting point of a unique *reduced trajectory* [i.e., the trajectory projected onto $\mathcal{B}(\mathbf{z}^e)$].

It is clear from Figs. 4 and 5 that the ICE manifold for the H_2/O system (with the selected reduced subspace $\mathcal{B}$) is not folded, and consequently for each reduced composition $\mathbf{r}$ there is exactly one corresponding manifold point which is denoted by $\mathbf{z}^{\mathrm{ICE}}(\mathbf{z}^e,\mathbf{r})$. That is, for each $\mathbf{r}\in\mathcal{B}^+(\mathbf{z}^e)$, the set

$$\mathbf{z}^{\mathrm{ICE}}(\mathbf{z}^e,\mathbf{r}) \equiv \{\mathbf{z}|\mathbf{z}\in\mathcal{M}^{\mathrm{ICE}}(\mathbf{z}^e,\mathbf{r}),\mathbf{B}^T\mathbf{z}=\mathbf{r}\} \tag{20}$$

consists of a single point.

Whether an ICE manifold is folded or not folded depends on the chemistry of the system, the values of $\mathbf{z}^e$, and the specified reduced subspace, *span*$(\mathbf{B})$. Our experience suggests that for typical combustion systems and a sensible specification of $\mathbf{B}$, ICE manifolds are not folded. Along a trajectory from a generating boundary point in $\partial\mathcal{M}^{\mathrm{CE}}(\mathbf{z}^e)$ to the equilibrium point $\mathbf{z}^{\mathrm{eq}}(\mathbf{z}^e)$, the tangent vectors of the ICE manifold are readily determined (from the sensitivity matrix $\mathbf{A}$). Hence a fold in the manifold along the trajectory can easily be detected [as a point where a tangent vector is orthogonal to *span*$(\mathbf{B})$].

An ICE manifold that is not folded has the following properties:

(1) **Invariance.** By construction, the ICE manifold is invariant.
(2) **Continuity and smoothness.** The constrained equilibrium edge $\partial\mathcal{M}^{\mathrm{CE}}(\mathbf{z}^e)$ is continuous, and it is smooth on each facet of the boundary $\partial\mathcal{C}^+(\mathbf{z}^e)$. The ICE manifold inherits these properties, and hence is continuous and piecewise smooth.
(3) **Consistency with fundamental laws.** The dynamics on the ICE manifold (like any invariant manifold) are those of the detailed kinetic system in the full composition space. As a consequence they are consistent with all fundamental laws, in particular, element conservation and the first and second laws of thermodynamics.
(4) **Existence of reconstructed species.** For every reduced composition $\mathbf{r}\in\mathcal{B}^+(\mathbf{z}^e)$ there exists a corresponding point $\mathbf{z}^{\mathrm{ICE}}$ on the ICE manifold (with $\mathbf{B}^T\mathbf{z}^{\mathrm{ICE}}=\mathbf{r}$).
(5) **Uniqueness of reconstructed species.** By definition of the ICE manifold being not folded, to every reduced composition $\mathbf{r}\in\mathcal{B}^+(\mathbf{z}^e)$ there exists a unique corresponding point on the ICE manifold $\mathbf{z}^{\mathrm{ICE}}(\mathbf{z}^e,\mathbf{r})$ [with $\mathbf{B}^T\mathbf{z}^{\mathrm{ICE}}(\mathbf{z}^e,\mathbf{r})=\mathbf{r}$].
(6) **Local determination.** As shown in the next section, for the given $\mathbf{z}^e$ and $\mathbf{r}$, the corresponding ICE manifold point $\mathbf{z}^{\mathrm{ICE}}(\mathbf{z}^e,\mathbf{r})$ can be determined without generating the whole manifold (or a significant portion of it).

[Properties (1)–(4) also apply to folded ICE manifolds.]

III. ICE-PIC: A METHOD TO DETERMINE POINTS ON THE ICE MANIFOLD USING THE CONSTRAINED EQUILIBRIUM PRE IMAGE CURVE

As illustrated in Fig. 4, for the idealized H_2/O system, the whole of the two-dimensional ICE manifold can be generated by following trajectories from the constrained equilibrium edge. However, computationally, the process of generating and representing the manifold rapidly becomes much more difficult, and soon infeasible, as the dimensionality n_r of the manifold increases. For the accurate reduced representation of the combustion chemistry of hydrocarbon fuels, manifolds of dimension $n_r>10$ may be required,[14,37] and the computational representation of a manifold of more than ten dimensions is surely infeasible.

Rather than the global method of generating the whole manifold, to apply the ICE manifold (with $n_r>10$, say) in practice for the dimension reduction of combustion chemistry, one needs instead a *local* method of species reconstruction; that is, a local method to determine the ICE manifold point $\mathbf{z}^{\mathrm{ICE}}(\mathbf{z}^e,\mathbf{r})$ for given values of $\mathbf{z}^e$ and $\mathbf{r}$. In this section we describe such a local method to determine points on the ICE manifold using the constrained equilibrium preimage curve, which we call the ICE-PIC method.

A. The preimage manifold

An important entity in the ICE-PIC method is the *preimage manifold* $\mathcal{M}^{\mathrm{PI}}(\mathbf{z}^e,\mathbf{r})$ introduced by Ren and Pope[25] and now described.

Given the reduced representation of the composition, $\{\mathbf{z}^e,\mathbf{r}\}$, the full composition is known to lie in the feasible region $\mathcal{F}(\mathbf{z}^e,\mathbf{r})$, Eq. (15). From each point $\hat{\mathbf{z}}$ in $\mathcal{F}(\mathbf{z}^e,\mathbf{r})$ the reaction trajectory can be followed backwards in time until [at time $-\tau^b(\hat{\mathbf{z}})$] it intersects the boundary $\partial\mathcal{C}^+(\mathbf{z}^e)$ at $\mathbf{z}^b(\hat{\mathbf{z}})$. The preimage manifold is defined to be the union of all of these trajectories:

$$\mathcal{M}^{\mathrm{PI}}(\mathbf{z}^e,\mathbf{r}) \equiv \{\mathbf{z}|\mathbf{z}=\mathbf{R}(\hat{\mathbf{z}},t),\hat{\mathbf{z}}\in\mathcal{F}(\mathbf{z}^e,\mathbf{r}),-\tau^b(\hat{\mathbf{z}})\leqslant t\leqslant 0\}. \tag{21}$$

For the idealized H_2/O system, Fig. 6 shows the feasible region and the preimage manifold that it generates. The

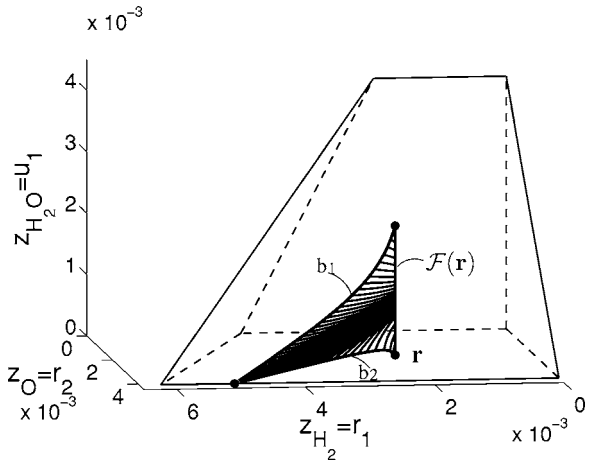

FIG. 6. Sketch showing the feasible region $\mathcal{F}(\mathbf{r})$ and the preimage manifold $\mathcal{M}^{\mathrm{PI}}$ corresponding to $\mathbf{r}=[z_{\mathrm{H_2}};z_{\mathrm{O}}]=[0.002\,12;0.002\,01]$ kmol/kg. The preimage manifold $\mathcal{M}^{\mathrm{PI}}$ intersects the boundary of the realizable region along the curves b_1 and b_2.

curves b_1 and b_2 are the boundaries of the preimage manifold, which are the intersections between the preimage manifold $\mathcal{M}^{\mathrm{PI}}(\mathbf{z}^e,\mathbf{r})$ and the boundaries of the realizable region $\mathcal{C}^+(\mathbf{z}^e,\mathbf{r})$. Curve b_1 is in the front facet and curve b_2 is in the reduced realizable region $\mathcal{B}^+(\mathbf{z}^e)$ (the lower facet).

Provided that the rate vector $\mathbf{S}(\hat{\mathbf{z}})$ has a nonzero component in the reduced subspace [i.e., $\mathbf{B}^T\mathbf{S}(\hat{\mathbf{z}})\neq 0$, for every $\hat{\mathbf{z}}\in\mathcal{F}(\mathbf{z}^e,\mathbf{r})$], then it follows from the well-known properties of ODEs that the dimension of the preimage manifold $\mathcal{M}^{\mathrm{PI}}(\mathbf{z}^e,\mathbf{r})$ is one more than the dimensionality of the feasible region $\mathcal{F}(\mathbf{z}^e,\mathbf{r})$ from which it is generated. That is, $\mathcal{M}^{\mathrm{PI}}(\mathbf{z}^e,\mathbf{r})$ is of dimension $(n_s-n_e-n_r+1)$. [If $\mathcal{F}(\mathbf{z}^e,\mathbf{r})$ contains the equilibrium point $\mathbf{z}^{\mathrm{eq}}(\mathbf{z}^e)$, then $\mathbf{z}^{\mathrm{eq}}(\mathbf{z}^e)$ is the corresponding point on the ICE manifold, and the ICE-PIC method to perform species reconstruction is not invoked. Otherwise (i.e., $\hat{\mathbf{z}}\neq\mathbf{z}^{\mathrm{eq}}$), the occurrence of $\mathbf{B}^T\mathbf{S}(\hat{\mathbf{z}})=0$ would indicate a very poor specification of the reduced subspace, *span*$(\mathbf{B})$.]

B. The constrained equilibrium preimage curve (CE-PIC)

By definition, a preimage curve is a curve lying in the preimage manifold with one end in the feasible region. Ren and Pope[25] describe a species-reconstruction technique based on the *minimum-curvature preimage curve*, which starts at the constrained equilibrium point $\mathbf{z}^{\mathrm{CE}}(\mathbf{z}^e,\mathbf{r})$, is initially tangent to the constrained equilibrium manifold (CEM), and is subsequently continued with minimum curvature. Here we consider another preimage curve which has two ends: one end in the feasible region and the other on the boundary of the realizable region.

The preimage curve considered here is defined by the property that every point on the curve is both a constrained equilibrium point and a preimage point. Thus, the CE-PIC denoted by $C^{\mathrm{CE}}(\mathbf{z}^e,\mathbf{r})$ is the intersection between the preimage manifold and the constrained equilibrium manifold:

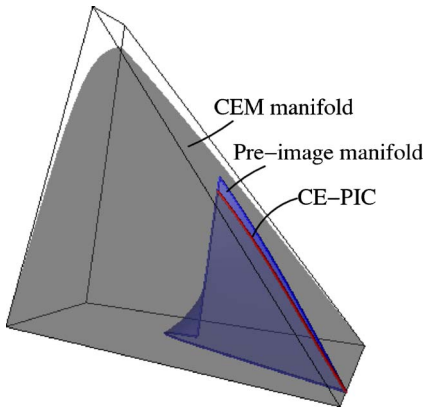

FIG. 7. Sketch showing the intersection between the CEM $\mathcal{M}^{\mathrm{CE}}(\mathbf{z}^e)$ and the preimage manifold $\mathcal{M}^{\mathrm{PI}}(\mathbf{z}^e,\mathbf{r})$ for $\mathbf{r}=[z_{\mathrm{H_2}};z_{\mathrm{O}}]=[0.002\,12;0.002\,01]$ kmol/kg. The intersection is the constrained equilibrium preimage curve (CE-PIC).

$$C^{\mathrm{CE}}(\mathbf{z}^e,\mathbf{r})\equiv\mathcal{M}^{\mathrm{PI}}(\mathbf{z}^e,\mathbf{r})\cap\mathcal{M}^{\mathrm{CE}}(\mathbf{z}^e). \tag{22}$$

Note that these two manifolds are of dimension $(n_s-n_e-n_r+1)$ and n_r, respectively, and so (provided that they are transverse), their intersection C^{CE} is one-dimensional (i.e., a curve) in the (n_s-n_e)-dimensional realizable region $\mathcal{C}^+(\mathbf{z}^e)$. It is important to appreciate that the CE-PIC is *not* a reaction trajectory since the CEM is not invariant.

For the idealized H_2/O system, Fig. 7 shows the CE-PIC which is the intersection between the CEM $\mathcal{M}^{\mathrm{CE}}(\mathbf{z}^e)$ and the preimage manifold $\mathcal{M}^{\mathrm{PI}}(\mathbf{z}^e,\mathbf{r})$, and Fig. 8 shows several related quantities.

The CE-PIC has two ends: the first, the feasible end, is the constrained equilibrium composition $\mathbf{z}^{\mathrm{CE}}(\mathbf{z}^e,\mathbf{r})$ (which is the intersection between the CEM and the feasible region). The second, the boundary end denoted $\mathbf{z}^g(\mathbf{z}^e,\mathbf{r})$, is the intersection of three objects: the CEM $\mathcal{M}^{\mathrm{CE}}$, the boundary $\partial\mathcal{C}^+(\mathbf{z}^e)$, and the preimage manifold $\mathcal{M}^{\mathrm{PI}}$. Being in $\mathcal{M}^{\mathrm{CE}}\cap\partial\mathcal{C}^+$ means that the point $\mathbf{z}^g(\mathbf{z}^e,\mathbf{r})$ is in the constrained equilibrium edge, and therefore also on the boundary of the ICE manifold. Therefore, the trajectory from $\mathbf{z}^g(\mathbf{z},\mathbf{r})$ is in the ICE manifold, and because $\mathbf{z}^g(\mathbf{z}^e,\mathbf{r})$ is a preimage point, this trajectory intersects the feasible region. It does so at the sought-after ICE manifold point $\mathbf{z}^{\mathrm{ICE}}(\mathbf{z}^e,\mathbf{r})$.

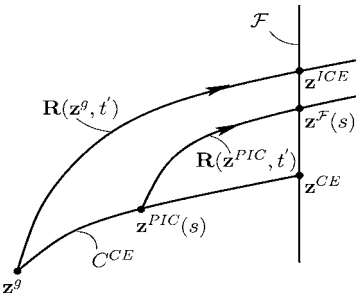

FIG. 8. Sketch showing (for given $\mathbf{z}^e$ and $\mathbf{r}$) the feasible region $\mathcal{F}(\mathbf{z}^e,\mathbf{r})$ and the constrained equilibrium preimage curve $C^{\mathrm{CE}}(\mathbf{z}^e,\mathbf{r})$. The general point on the CE-PIC is denoted by $\mathbf{z}^{\mathrm{PIC}}(\mathbf{z}^e,\mathbf{r},s)$, and the reaction trajectory from it, $\mathbf{R}(\mathbf{z}^{\mathrm{PIC}},t')$, intersects the feasible region at $\mathbf{z}^{\mathcal{F}}(\mathbf{z}^e,\mathbf{r},s)=\mathbf{R}(\mathbf{z}^{\mathrm{PIC}},t(s))$. The feasible end of the CE-PIC is $\mathbf{z}^{\mathrm{PIC}}(\mathbf{z}^e,\mathbf{r},0)=\mathbf{z}^{\mathrm{CE}}(\mathbf{z}^e,\mathbf{r})$ and the boundary end is $\mathbf{z}^g(\mathbf{z}^e,\mathbf{r})=\mathbf{z}^b(\mathbf{z}^{\mathrm{ICE}})$. The reaction trajectory from $\mathbf{z}^g$ is in the ICE manifold, and it intersects the feasible region at $\mathbf{z}^{\mathrm{ICE}}(\mathbf{z}^e,\mathbf{r})=\mathbf{R}(\mathbf{z}^g,\tau^b(s^b))=\mathbf{z}^{\mathcal{F}}(\mathbf{z}^e,\mathbf{r},s^b)$ after time $\tau^b(\mathbf{z}^{\mathrm{ICE}})$.

Thus the boundary end $\mathbf{z}^g(\mathbf{z}^e,\mathbf{r})$ of the CE-PIC is the generating boundary point of the ICE manifold corresponding to the reduced composition $\mathbf{r}$, i.e.,

$$\mathbf{z}^{\mathrm{ICE}}(\mathbf{z}^e,\mathbf{r}) = \mathbf{R}(\mathbf{z}^g(\mathbf{z}^e,\mathbf{r}),\tau^b(\mathbf{z}^{\mathrm{ICE}})), \tag{23}$$

$$\mathbf{z}^g(\mathbf{z}^e,\mathbf{r}) = \mathbf{R}(\mathbf{z}^{\mathrm{ICE}}(\mathbf{z}^e,\mathbf{r}),-\tau^b(\mathbf{z}^{\mathrm{ICE}})) = \mathbf{z}^b(\mathbf{z}^{\mathrm{ICE}}(\mathbf{z}^e,\mathbf{r})), \tag{24}$$

where τ^b is the time along the reaction trajectory from $\mathbf{z}^g(\mathbf{z}^e,\mathbf{r})$ to $\mathbf{z}^{\mathrm{ICE}}(\mathbf{z}^e,\mathbf{r})$, which is in the feasible region.

The CE-PIC can be naturally parametrized by the arclength s measured from the feasible end $\mathbf{z}^{\mathrm{CE}}(\mathbf{z}^e,\mathbf{r})$. We denote the general point on the CE-PIC $C^{\mathrm{CE}}(\mathbf{z}^e,\mathbf{r})$ by $\mathbf{z}^{\mathrm{PIC}}(\mathbf{z}^e,\mathbf{r},s)$, or simply $\mathbf{z}^{\mathrm{PIC}}(s)$. The time along the reaction trajectory from the point $\mathbf{z}^{\mathrm{PIC}}(\mathbf{z}^e,\mathbf{r},s)$ on the CE-PIC curve to the feasible region is denoted by $t(\mathbf{z}^e,\mathbf{r},s)$, or simply $t(s)$. As sketched in Fig. 8, after time $t(s)$, the reaction trajectory from $\mathbf{z}^{\mathrm{PIC}}(s)$ intersects the feasible region at a *feasible point* denoted by $\mathbf{z}^{\mathcal{F}}(\mathbf{z}^e,\mathbf{r},s)$ or simply $\mathbf{z}^{\mathcal{F}}(s)$. Thus for $0 \leqslant s \leqslant s^b$ [where $s^b(\mathbf{z}^e,\mathbf{r})$ is the arclength at the boundary end $\mathbf{z}^g(\mathbf{z}^e,\mathbf{r})$] we have

$$\mathbf{z}^{\mathcal{F}}(\mathbf{z}^e,\mathbf{r},s) = \mathbf{R}(\mathbf{z}^{\mathrm{PIC}}(\mathbf{z}^e,\mathbf{r},s),t(s)). \tag{25}$$

The feasible end of the CE-PIC is

$$\mathbf{z}^{\mathrm{PIC}}(\mathbf{z}^e,\mathbf{r},0) = \mathbf{z}^{\mathrm{CE}}(\mathbf{z}^e,\mathbf{r}), \tag{26}$$

and $\mathbf{z}^{\mathcal{F}}(0)$ is coincident with this point. The boundary end of the CE-PIC is

$$\mathbf{z}^{\mathrm{PIC}}(\mathbf{z}^e,\mathbf{r},s^b(\mathbf{z}^e,\mathbf{r})) = \mathbf{z}^g(\mathbf{z}^e,\mathbf{r}) = \mathbf{z}^b(\mathbf{z}^{\mathrm{ICE}}), \tag{27}$$

and the corresponding feasible point is

$$\mathbf{z}^{\mathcal{F}}(s^b) = \mathbf{z}^{\mathrm{ICE}}(\mathbf{z}^e,\mathbf{r}). \tag{28}$$

C. The ICE-PIC method

Given the reduced representation, $\{\mathbf{z}^e,\mathbf{r}\}$, the ICE-PIC method achieves species reconstruction by identifying the corresponding point on the ICE manifold, $\mathbf{z}^{\mathrm{ICE}}(\mathbf{z}^e,\mathbf{r})$. A literal implementation of the ideas developed above leads to the following three-step algorithm.

(1) The constrained equilibrium composition $\mathbf{z}^{\mathrm{CE}}(\mathbf{z}^e,\mathbf{r})$ is computed, e.g., by the constraint potential method.
(2) The CE-PIC is followed from its feasible end $\mathbf{z}^{\mathrm{PIC}}(0) = \mathbf{z}^{\mathrm{CE}}(\mathbf{z}^e,\mathbf{r})$ to its boundary end $\mathbf{z}^{\mathrm{PIC}}(s^b) = \mathbf{z}^g(\mathbf{z}^e,\mathbf{r})$.
(3) The reaction trajectory from $\mathbf{z}^g(\mathbf{z}^e,\mathbf{r})$ is followed forward in time until it intersects the feasible region at $\mathbf{z}^{\mathcal{F}}(s^b) = \mathbf{z}^{\mathrm{ICE}}(\mathbf{z}^e,\mathbf{r})$.

Provided that the CE-PIC exists (i.e., that the CEM and preimage manifolds are transverse), each of these steps can be reliably performed, thus ensuring the success of the method to identify the unique ICE manifold point, $\mathbf{z}^{\mathrm{ICE}}(\mathbf{z}^e,\mathbf{r})$.

As mentioned, the first step can be efficiently performed using the constraint potential method.[31] In essence, the n_e+n_r constraint potentials $\boldsymbol{\lambda}$ are determined by the n_e+n_r equations $\mathbf{E}^T\mathbf{z}=\mathbf{z}^e$ and $\mathbf{B}^T\mathbf{z}=\mathbf{r}$.

The second step can be performed by traversing the CE-PIC in small steps using a combination of the methods described by Ren and Pope[25] and Pope.[31] At arclength s along the curve, the constraint potentials are $\boldsymbol{\lambda}(s)$, and the constrained equilibrium composition determined by $\boldsymbol{\lambda}$ is $\mathbf{z}^{\mathrm{PIC}}(\mathbf{z}^e,\mathbf{r},s)$. (The use of the constraint potential method forces the composition to remain on the constrained equilibrium manifold.) For small Δs, the n_e+n_r constraint potentials $\boldsymbol{\lambda}(s+\Delta s)$ and the time $t(s+\Delta s)$ are determined from the (n_e+n_r+1) simultaneous equations as follows:

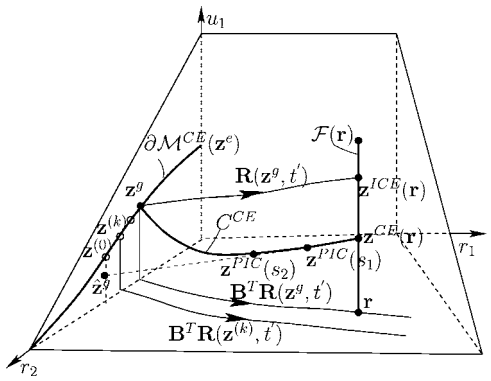

FIG. 9. For a case with two represented variables (r_1 and r_2) and one unrepresented variable (u_1), a sketch of the realizable region $\mathcal{C}^+(\mathbf{z}^e)$ showing the feasible region $\mathcal{F}(\mathbf{r})$ and the constrained equilibrium point $\mathbf{z}^{\mathrm{CE}}(\mathbf{r})$, corresponding to the given reduced composition $\mathbf{r}$; the constrained equilibrium preimage curve C^{CE} from $\mathbf{z}^{\mathrm{CE}}$ to its boundary end $\mathbf{z}^g$, which lies in a facet of $\partial\mathcal{C}^+(\mathbf{z}^e)$ (the triangle at the left, on which r_1 is zero); the constrained equilibrium edge $\partial\mathcal{M}^{\mathrm{CE}}(\mathbf{z}^e)$ in this facet; and the trajectory $\mathbf{R}(\mathbf{z}^g,t')$, which intersects the feasible region at $\mathbf{z}^{\mathrm{ICE}}$. Based on the two CE-PIC points $\mathbf{z}^{\mathrm{PIC}}(s_1)$ and $\mathbf{z}^{\mathrm{PIC}}(s_2)$, a predicted value $\hat{\mathbf{z}}^g$ of $\mathbf{z}^g$ is obtained by extrapolation to the facet. A Newton iteration is performed yielding a succession of estimates $[\mathbf{z}^{(0)},\mathbf{z}^{(1)},\ldots,\mathbf{z}^{(k)},\ldots]$ of $\mathbf{z}^g$ [all in $\partial\mathcal{M}^{\mathrm{CE}}(\mathbf{z}^e)$]. The initial guess $\mathbf{z}^{(0)}$ has the same value of the represented variables as $\hat{\mathbf{z}}^g$, and the iteration is based on refining $\mathbf{z}^{(k)}$ with the aim of making the projected reaction trajectory $\mathbf{B}^T\mathbf{R}(\mathbf{z}^{(k)},t')$ pass through $\mathbf{r}$.

$$\mathbf{E}^T\mathbf{z}^{\mathrm{PIC}} = \mathbf{z}^e, \tag{29}$$

$$\mathbf{B}^T\mathbf{R}(\mathbf{z}^{\mathrm{PIC}}(\mathbf{z}^e,\mathbf{r},s+\Delta s),t(s+\Delta s)) = \mathbf{r}, \tag{30}$$

and

$$|\mathbf{z}^{\mathrm{PIC}}(\mathbf{z}^e,\mathbf{r},s+\Delta s) - \mathbf{z}^{\mathrm{PIC}}(\mathbf{z}^e,\mathbf{r},s)| = \Delta s, \tag{31}$$

where $|\mathbf{z}|$ denotes the two-norm $(\mathbf{z}^T\mathbf{z})^{1/2}$. The first of these equations imposed the elemental composition; the second is the requirement that $\mathbf{z}^{\mathrm{PIC}}(\mathbf{z}^e,\mathbf{r},s+\Delta s)$ is a preimage point; and the third is the definition of the arclength increment.

The above applies in the interior of $\mathcal{C}^+(\mathbf{z}^e)$. As the curve reaches the boundary $\partial\mathcal{C}^+(\mathbf{z}^e)$, the species specific moles z_i of some species tend to zero, and correspondingly a constraint potential tends to minus infinity. To avoid the associated difficulties, the curve is extrapolated to the boundary to predict $\mathbf{z}^g(\mathbf{z}^e,\mathbf{r})$ and the facet in which it lies. Figure 9 illustrates the process by which the two CE-PIC points $\mathbf{z}^{\mathrm{PIC}}(s_1)$ and $\mathbf{z}^{\mathrm{PIC}}(s_2)$ are used to construct an estimate $\hat{\mathbf{z}}^g$ of the boundary end of the CE-PIC, $\mathbf{z}^g$. On the facet thus identified, the reduced composition $\mathbf{r}$ has n_r-1 degrees of freedom, and, with the absent species removed from consideration, the constrained equilibrium composition is determined by the (n_e+n_r-1) remaining constraint potentials. The estimate $\hat{\mathbf{z}}^g$ of $\mathbf{z}^g(\mathbf{z}^e,\mathbf{r})$ can be improved by a Newton iteration in which the (n_e+n_r) unknowns are the (n_e+n_r-1) constraint potentials and the time $t=\tau^b$ along the trajectory to the feasible region, and the

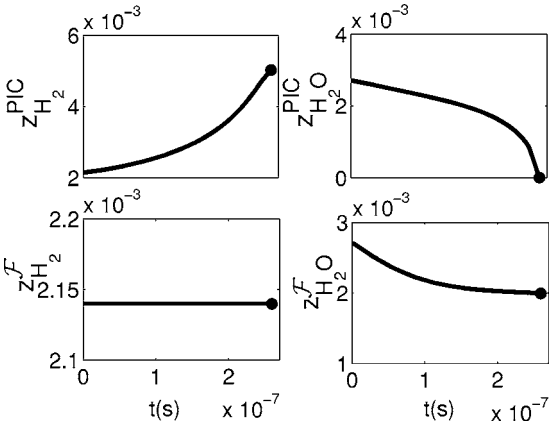

FIG. 10. Top row: composition $\mathbf{z}^{\mathrm{PIC}}(t)$ along the CE-PIC with $\mathbf{r}=[z_{\mathrm{H}_2};z_{\mathrm{O}}]=[0.002\,14;0.000\,929]$ kmol/kg; the dot is the boundary end of the CE-PIC, $\mathbf{z}^g=\mathbf{z}^{\mathrm{PIC}}(\tau^b)$, where $\tau^b=2.60\times10^{-7}$ s. Bottom row: the feasible composition $\mathbf{z}^{\mathcal{F}}(t)$ mapped from the CE-PIC for the same case; the dot is the reconstructed composition $\mathbf{z}^{\mathrm{ICE}}=\mathbf{z}^{\mathcal{F}}(\tau^b)$ on the ICE manifold.

(n_e+n_r) equations are analogous to Eqs. (29) and (30). After k iterations, the estimate of $\mathbf{z}^g(\mathbf{z}^e,\mathbf{r})$ is denoted by $\mathbf{z}^{(k)}$. The initial estimate $\mathbf{z}^{(0)}$ is the constrained equilibrium point with the same value of the represented variables as $\hat{\mathbf{z}}^g$. As illustrated in Fig. 9, the iterate $\mathbf{z}^{(k)}$ is determined by a linear approximation to the requirement that the projected reaction trajectory $\mathbf{B}^T\mathbf{R}(\mathbf{z}^{(k)},t')$ passes through $\mathbf{r}$ [or equivalently that $\mathbf{R}(\mathbf{z}^{(k)},t')$ intersects $\mathcal{F}(\mathbf{r})$].

Once $\mathbf{z}^g(\mathbf{z}^e,\mathbf{r})$ has been determined in step (2), then step (3) in principle requires the integration of the ODEs $d\mathbf{z}/dt=\mathbf{S}(\mathbf{z})$ from the initial condition $\mathbf{z}^g$ along the reaction trajectory until the feasible region is reached to yield $\mathbf{z}^{\mathrm{ICE}}(\mathbf{z}^e,\mathbf{r})$. In practice, this integration has already been performed as part of the iteration in step (2).

The method requires $\mathbf{z}^g(\mathbf{z}^e,\mathbf{r})$ to be accurately determined—as it is by the Newton iteration performed on the facet. But the CE-PIC does not have to be traversed accurately: all that is required is an estimate of $\mathbf{z}^g$, which is sufficiently accurate for the Newton iteration on the facet to converge. For the sake of efficiency, we therefore evaluate as few points on the CE-PIC as possible, and, as necessary, repeatedly extrapolate to the boundary and attempt the Newton iteration. In practice, the computation of three or four points on the CE-PIC is usually sufficient. In anticipation of combining the ICE-PIC method with ISAT, we observe also that infinitesimal changes in the reconstructed composition, i.e., $\mathbf{z}^{\mathrm{ICE}}(\mathbf{z}^e+d\mathbf{z}^e,\mathbf{r}+d\mathbf{r})$, can be determined from the CEM at $\mathbf{z}^g$ and from the sensitivity matrix $\mathbf{A}(\mathbf{z}^g,\tau^b)$. A knowledge of the CE-PIC is not needed.

For all the cases we have performed, $t(s)$ increases monotonically with the arclength s along the CE-PIC. Therefore, for such cases the CE-PIC can be equivalently parametrized by t, i.e., $\mathbf{z}^{\mathrm{PIC}}(t)$. For the idealized H_2/O system, for $\mathbf{r}=[0.002\,14;0.000\,929]$ kmol/kg, Fig. 10 shows the composition $\mathbf{z}^{\mathrm{PIC}}(t)$ along the CE-PIC. As may be seen from the figure, $\mathbf{z}^{\mathrm{PIC}}$ changes significantly along the curve. The dot in the figure is the ending point of the curve, that is, the generating boundary point $\mathbf{z}^g(\mathbf{z}^e,\mathbf{r})$. The species specific moles $z^{\mathrm{PIC}}_{\mathrm{H_2O}}$ and $z^{\mathrm{PIC}}_{\mathrm{H}}$ of the generating boundary point are zero. Figure 10 also shows the feasible composition $\mathbf{z}^{\mathcal{F}}(t)$ mapped from the preimage curve. Since H_2 is the represented species, inevitably, we have a constant value of $z^{\mathcal{F}}_{\mathrm{H}_2}(t)$ even though $z^{\mathrm{PIC}}_{\mathrm{H}_2}(t)$ varies appreciably. For the unrepresented species, it may be seen that they approach asymptotic values due to the fact that trajectories from the latter part of the CE-PIC have been attracted to a low-dimensional manifold. The dot in the figure is the corresponding point on the ICE manifold $\mathbf{z}^{\mathrm{ICE}}(\mathbf{z}^e,\mathbf{r})$.

IV. ICE-PIC METHOD FOR ADIABATIC SYSTEMS

In this section, we discuss the differences between adiabatic and isothermal systems and indicate the necessary changes in order to apply the ICE-PIC method to adiabatic systems.

For a closed, homogeneous, adiabatic, and isobaric reacting system, conserved quantities (fixed for all time) are the mass m, the pressure p, the specific enthalpy h, and the element specific moles $\mathbf{z}^e$. The state of the system is completely specified by p, h, and $\mathbf{z}$. And the ICE-PIC method approximates the dynamics of the system by $\{p,h,\mathbf{z}^e,\mathbf{r}\}$.

The specific enthalpy of the system, h, is related to the temperature T by

$$h=\mathbf{z}^T\bar{\mathbf{h}}(T), \tag{32}$$

where $\bar{h}_i(T)$ is the molar specific enthalpy of species i, which is a strictly increasing function of T. Below some temperature T_{low}, the ideal gas assumption and the accuracy of the chemical kinetics break down. Accordingly, for the adiabatic case, the definition [Eq. (4)] of the realizable region is modified to exclude compositions $\mathbf{z}$ at which the temperature is below T_{low}—or, equivalently, at which the enthalpy h is less than $\mathbf{z}^T\bar{\mathbf{h}}(T_{\mathrm{low}})$:

$$\mathcal{C}^+(\mathbf{z}^e,h)=\{\mathbf{z}|z_i\geqslant 0,\mathbf{z}^T\bar{\mathbf{h}}(T_{\mathrm{low}})\leqslant h,\mathbf{E}^T\mathbf{z}=\mathbf{z}^e,\mathbf{z}\in\mathcal{C}\}. \tag{33}$$

Note that the constraint on temperature appears as a linear inequality constraint on $\mathbf{z}$, and hence $\mathcal{C}^+(\mathbf{z}^e,h)$ is a convex polytope, as in the isothermal case.

Among all thermodynamic variables defined in $\mathcal{C}^+(\mathbf{z}^e,h)$, of particular interest is the entropy $\mathcal{S}(\mathbf{z})$, which is strictly concave and has a unique global maximum in the interior of $\mathcal{C}^+(\mathbf{z}^e,h)$. For the adiabatic, isobaric system considered, the location of this maximum corresponds to chemical equilibrium. Due to chemical reactions, the composition $\mathbf{z}(t)$ evolves in time t according to a set of ODEs similar to Eq. (5). The enthalpy along the reaction trajectory remains constant, whereas the temperature varies. The reaction rate vector $\mathbf{S}$ has all the properties listed in Sec. II D, except now the second law of thermodynamics and the law of mass action force the entropy to increase with time along a reaction trajectory until equilibrium is reached (instead of the Gibbs function decreasing).

Given p, h, $\mathbf{z}^e$, and $\mathbf{r}$, the corresponding point on the CEM for the adiabatic system is the point in the feasible region at which entropy is maximum (in contrast to the Gibbs function being minimum in the isothermal system).

All of the other concepts, such as the constrained equilibrium edge, the ICE manifold, the preimage manifold, and the CE-PIC curve, are the same as for the isothermal system. With small modifications, the ICE-PIC method developed in Sec. III can therefore be applied to adiabatic systems.

V. COMPARATIVE TESTING OF SPECIES RECONSTRUCTION METHODOLOGIES

In this section, the ability of the ICE-PIC method of species reconstruction is investigated for the test case of a hydrogen/air premixed laminar flame, and quantitative comparisons are made with other methodologies, namely, RCCE, ILDM, and QSSA. As described fully in Sec. V A, using a detailed chemical mechanism for hydrogen, the one-dimensional steady laminar flame equations are solved to yield profiles of the full composition as a function of the distance x, denoted by $\mathbf{z}^P(x)$, through the flame. At any point in the flame, the reduced composition can be deduced from $\mathbf{z}^P(x)$ and, based on this, one of the species-reconstruction methods can be used to yield an estimate $\mathbf{z}^{\mathcal{M}}(x)$ for the full composition. Then the resulting error in the species reconstruction, $\mathbf{z}^P(x)-\mathbf{z}^{\mathcal{M}}(x)$, can be examined and quantified.

For a given choice of represented variables, all the dimension-reduction methodologies considered (i.e., ICE-PIC, RCCE, ILDM, and QSSA) identify attracting manifolds based solely on chemical kinetics and thermodynamics. In the laminar flame equations, one effect of molecular diffusion is to draw compositions away from these attracting manifolds.[38] Hence the difference $\mathbf{z}^P(x)-\mathbf{z}^{\mathcal{M}}(x)$ is in part due to this effect of molecular diffusion.

In the following subsections we describe the premixed laminar flame computations and the four species reconstructions methodologies, and then the results are reported.

A. Computations of a premixed laminar flame

The test case considered is the steady, isobaric, adiabatic, one-dimensional premixed laminar flame of a pure stoichiometric hydrogen/air mixture with an unburnt temperature of 300 K and pressure of 1 atm. The detailed chemical mechanism employed is the mechanism of Li *et al.*,[29] which involves three elements, nine species, and 21 reactions. Nitrogen chemistry is not included so that N_2 is considered to be inert.

The governing partial differential equations for the one-dimensional flame are solved using Sandia's PREMIX code with full multicomponent transport properties of the species. The resulting profiles of temperature, $T^P(x)$, and the species specific moles, $\mathbf{z}^P(x)$, are shown in Figs. 11 and 12 as functions of distance x. As may be seen from the figures, the consumption of hydrogen and formation of water occurs in a very thin reaction zone. Besides plotting the results against the distance x across the flame, another more revealing way is to show the results against the temperature $T^P(x)$. [All the quantities such as $\mathbf{z}^P(x)$ and $\mathbf{z}^P(x)-\mathbf{z}^{\mathcal{M}}(x)$ can be parametrized by $T^P(x)$, which is an increasing function of distance x through the flame.] In the following, we mainly use the latter to show the test results.

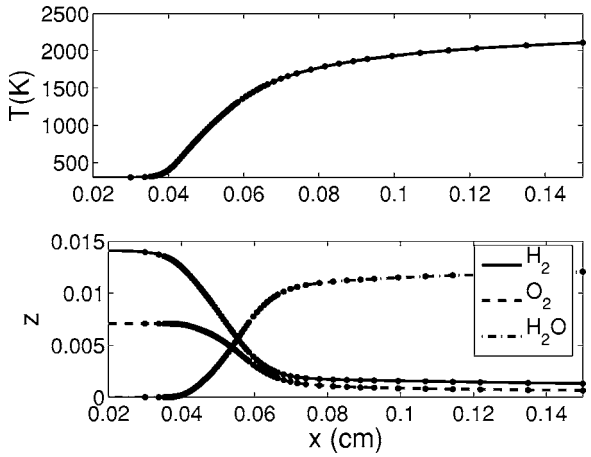

FIG. 11. Temperature and species specific moles across the flame. Lines: composition $(T^P,\mathbf{z}^P)$ obtained using PREMIX with detailed chemistry; dots: compositions $(T^{\mathrm{ICE}},\mathbf{z}^{\mathrm{ICE}})$ reconstructed using the ICE-PIC method.

B. Species reconstruction using ICE-PIC

At different locations across the flame, the adiabatic ICE-PIC method is employed to perform species reconstruction, i.e., to determine the full composition $\mathbf{z}^{\mathrm{ICE}}$ on the corresponding ICE manifold as an estimate of $\mathbf{z}^P$. At each location, the thermochemical state is completely specified by pressure p, specific enthalpy h, and the species specific

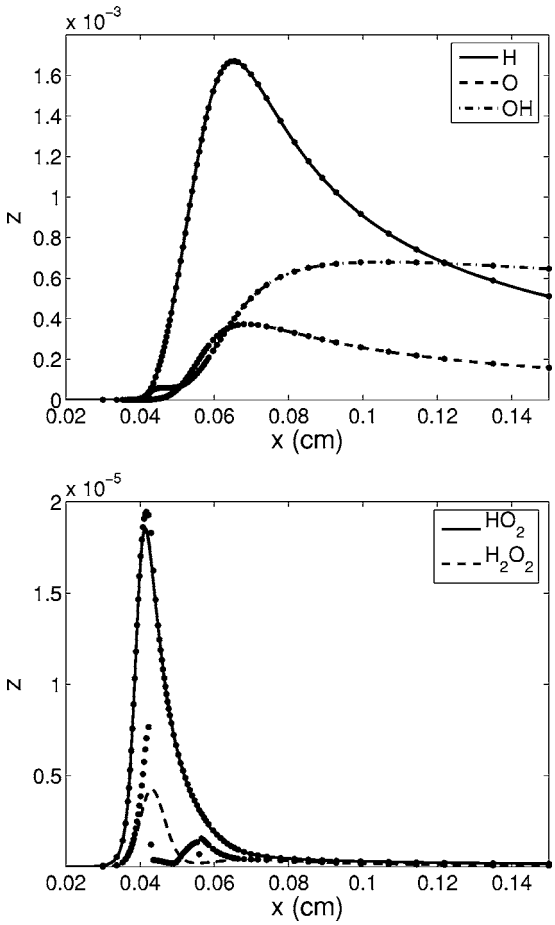

FIG. 12. Species specific moles across the flame. Lines: composition $(\mathbf{z}^P)$ obtained using PREMIX with detailed chemistry; dots: composition $(\mathbf{z}^{\mathrm{ICE}})$ reconstructed using the ICE-PIC method.

moles $\mathbf{z}$; and given the reduced representation $\{\mathbf{z}^e, h, \mathbf{r}\}$, the ICE-PIC method is applied to the corresponding adiabatic, isobaric closed system. In this application, we take $n_r=4$, and specify the reduced compositions $\mathbf{r}$ to be the specific moles of the species H_2, O_2, H_2O, and H. Thus with the given $\mathbf{z}^e$ and h, the dimensionality of the low-dimensional manifolds is 4. At each location, the species specific moles of the represented species $\mathbf{r}$, the element specific moles $\mathbf{z}^e$, and enthalpy are extracted from the full composition $\{h, \mathbf{z}^P\}$ obtained using PREMIX with the detailed mechanism. The reconstructed composition on the ICE manifold $\mathbf{z}^{\mathrm{ICE}}(\mathbf{z}^e, h, \mathbf{r})$ is then obtained using the ICE-PIC method. The value $T_{\mathrm{low}}=280$ K is specified, but the lowest temperature encountered is greater than this, and so the restriction $T \geqslant T_{\mathrm{low}}$ has no effect in this case. (In other cases, e.g., with $n_r=2$, this bound is encountered.)

The reconstructed composition $\mathbf{z}^{\mathrm{ICE}}$ and temperature T^{ICE} obtained using ICE-PIC are also shown (as dots) in Figs. 11 and 12. The represented species are, of course, reconstructed without error. For the unrepresented radicals O and OH, there is no noticeable difference between $\mathbf{z}^{\mathrm{ICE}}$ and $\mathbf{z}^P$. There is also good agreement for temperature, with the normalized error [defined as $\epsilon_T=(2\times|T^{\mathrm{ICE}}-T^P)/(T^{\mathrm{ICE}}+T^P)$] being less than 1.5×10^{-3} across the whole flame. There are noticeable differences in the unrepresented species HO_2 and more so in H_2O_2, see Fig. 12. These differences are partly due to the effect of molecular diffusion. (For RCCE, ILDM, and QSSA, we also observe large errors in H_2O_2.) However, these differences do not affect the chemical dynamics for the represented species, as is shown below.

C. Species reconstruction using RCCE

In the ICE-PIC method, the constrained equilibrium manifold is used only to identify the constrained equilibrium edge. In contrast, in the RCCE approach to simplify chemical kinetics, the CEM is taken as the low-dimensional attracting manifold. With the same reduced representation as in the ICE-PIC method, the composition on the CEM manifold can be determined. (Indeed, this is the first step of the ICE-PIC method.) Figure 13 (plotted against the temperature T^P) compares the reconstructed compositions on both the ICE and CEM manifolds together with $\mathbf{z}^P$. As may be seen from the figure, for the unrepresented radicals O and OH, there is a significant difference between $\mathbf{z}^{\mathrm{RCCE}}$ and $\mathbf{z}^P$ in the temperature range of 600–1900 K, where the chemical kinetics are important. In comparison, as previously noted, there is excellent agreement between $\mathbf{z}^{\mathrm{ICE}}$ and $\mathbf{z}^P$. The reason for this difference is that the CEM manifold is fully based on the thermodynamics, taking no account of the chemical kinetics, whereas the ICE-PIC method accounts for the chemical kinetics by following the reaction trajectories.

D. Species reconstruction using ILDM

By definition, the ILDM is the set of compositions $\mathbf{z}$ satisfying

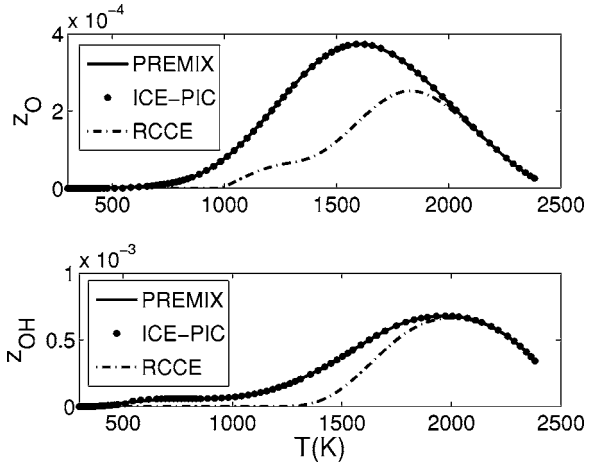

FIG. 13. Species specific moles across the flame. Lines: $\mathbf{z}^P$ from PREMIX; dots: $\mathbf{z}^{\mathrm{ICE}}$ from ICE-PIC; dot-dashed line: $\mathbf{z}^{\mathrm{CEM}}$. The profiles are plotted against the temperature $T^P(x)$, which is an increasing function of distance x through the flame.

$$\mathbf{U}_f^T\mathbf{S}(\mathbf{z})=0, \tag{34}$$

where $\mathbf{S}(\mathbf{z})$ is the rate vector and $span(\mathbf{U}_f)$ is the fast subspace of the Jacobian matrix $\mathbf{J}(\mathbf{z})$ (see Ref. 20 for further details). Given the same reduced representation $\{\mathbf{z}^e, h, \mathbf{r}\}$ as in the ICE-PIC method, species reconstruction using ILDM consists of identifying ILDM compositions $\mathbf{z}^{\mathrm{ILDM}}$ satisfying Eq. (34) in the feasible region $\mathcal{F}(\mathbf{z}^e, h, \mathbf{r})$.

While the existence and uniqueness of the reconstructed composition are guaranteed by RCCE and ICE-PIC (for an unfolded ICE manifold), there are no such guarantees with ILDM. Figure 14 shows $z^{\mathrm{ILDM}}_{H_2O_2}$ compared to $z^P_{H_2O_2}$ for the premixed laminar flame. As may be seen, there is excellent agreement at high temperature, with no discernible differences down to 1600 K. As the temperature decreases further, there is a clear divergence between $\mathbf{z}^{\mathrm{ILDM}}_{H_2O_2}$ and $z^P_{H_2O_2}$; and below 1200 K, $z^{\mathrm{ILDM}}_{H_2O_2}$ decreases almost linearly to reach zero (with nonzero slope) around 875 K. (The value of $z^{\mathrm{ILDM}}_{H_2O_2}$ ob-

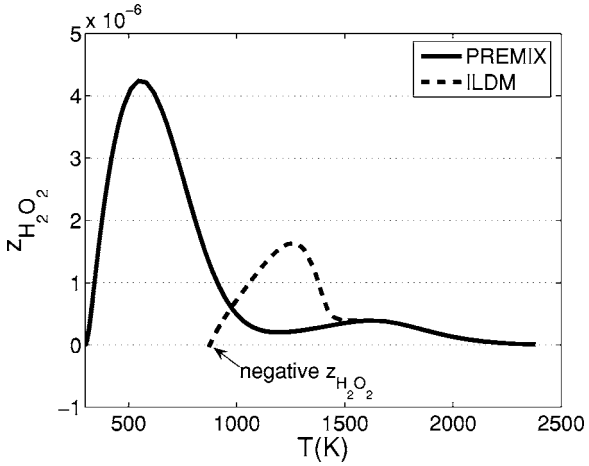

FIG. 14. Species specific moles of $z_{H_2O_2}$. Solid line: $z^P_{H_2O_2}$ obtained using PREMIX with detailed chemistry; dashed line: $z^{\mathrm{ILDM}}_{H_2O_2}$, reconstructed using ILDM. Note that $z^{\mathrm{ILDM}}_{H_2O_2}$ passes through zero at about $T=875$ K. The profiles are plotted against the temperature $T^P(x)$, which is an increasing function of distance x through the flame.

tained at 871.24 K is -3.6×10^{-8} kmol/kg.) Below this temperature we are unable to find ILDM points in the feasible region $\mathcal{F}(\mathbf{z}^e,h,\mathbf{r})$. These findings are consistent with the ILDM not existing below 875 K for this case.

E. Species reconstruction using QSSA

In ICE-PIC, RCCE, and ILDM, the same reduced representation $\{\mathbf{z}^e,h,\mathbf{r}\}$ is used, and hence these three methods can be compared directly. In QSSA, on the other hand, the reduced representation is $\{h,\mathbf{r}\}$, with no information about the elemental composition of the unrepresented species. As a consequence, the comparison with QSSA is somewhat less direct.

In the other methods there are eight degrees of freedom in the reduced representation (enthalpy, three elements, four represented species). We consider, therefore, a standard QSSA method[39] with the same number of degrees of freedom, specifically, enthalpy and the specific moles of seven major (i.e., non-steady-state) species: H_2, O_2, H_2O, H, OH, O, and N_2. The quasi-steady-state assumption is applied to the two minor species HO_2 and H_2O_2. Given that there are three elements in the system, the dimensionality of the low-dimensional manifolds of the QSSA method is $7-3=4$. With the values of the major species specific moles being taken from $\mathbf{z}^P$, the minor species are reconstructed from the quasi-steady-state approximation. (This specification for the major species favors QSSA in later comparisons because of the omission of errors in two additional major species, OH and O.)

F. Comparison of species reconstruction errors

Let $\mathbf{z}^{\mathcal{M}}$ denote the reconstructed species specific moles using one of the methods described in the preceding four subsections (i.e., $\mathbf{z}^{\mathcal{M}}$ is one of $\mathbf{z}^{\mathrm{ICE}}$, $\mathbf{z}^{\mathrm{RCCE}}$, $\mathbf{z}^{\mathrm{ILDM}}$, or $\mathbf{z}^{\mathrm{QSSA}}$). Then, as a function of position through the flame, we define the normalized species-reconstruction error as

$$\varepsilon_z=\frac{2\times|\mathbf{z}^{\mathcal{M}}-\mathbf{z}^P|}{|\mathbf{z}^{\mathcal{M}}|+|\mathbf{z}^P|}. \tag{35}$$

The reconstruction errors for all four species reconstruction methodologies are shown in Fig. 15 (plotted against temperature T^P). Considering first temperatures above 875 K, it is readily observed that RCCE incurs much larger errors than all other methods with a peak of $\varepsilon_z^{\mathrm{RCCE}}=0.015$ at $T=1450$ K. In this range ($T>875$ K), all other methods yield very small errors (less than 1.2×10^{-4}), with $\varepsilon_z^{\mathrm{ICE}}$ being very similar to $\varepsilon_z^{\mathrm{ILDM}}$.

Below 875 K, the ILDM does not exist, while QSSA yields large errors $\varepsilon_z^{\mathrm{QSSA}}$ as the low-temperature boundary is approached ($T=300$ K). On the other hand, for ICE-PIC and RCCE the errors are here well controlled. This is because the specific moles of elements in the unrepresented species are very small, and hence the specific moles of the unrepresented species are small, thus limiting the maximum possible error. In contrast, in QSSA, spuriously large values of minor species can occur.

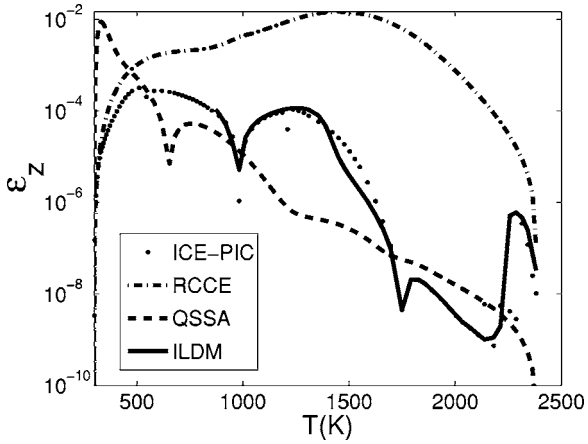

FIG. 15. Normalized errors [Eq. (35)] in reconstructed compositions. The profiles are plotted against the temperature $T^P(x)$, which is an increasing function of distance x through the flame.

Of the species reconstruction methodologies that succeed over the entire temperature range, ICE-PIC yields the smallest maximum error: over the whole range $\varepsilon_z^{\mathrm{ICE}}$ is less than 3×10^{-4}.

Besides the reconstructed composition, it is also important to study the reconstructed rate vector [i.e., $\mathbf{S}(\mathbf{z}^{\mathcal{M}})$] and to compare it to $\mathbf{S}(\mathbf{z}^P)$. Figure 16 (plotted against temperature T^P) compares the rates for H_2O for all four species-reconstruction methodologies together with $S_{H_2O}(\mathbf{z}^P)$. As may be seen from the figure, the composition on the CEM manifold has qualitatively different chemical kinetics compared to all others. This is due to the inaccurate reconstruction of the important O and OH species on the CEM manifold (see Fig. 13). In comparison, the reconstructed rates of H_2O using ICE-PIC, QSSA, and ILDM all have good quantitative agreement with $S_{H_2O}(\mathbf{z}^P)$. (The ILDM is not able to predict the chemical kinetics below 875 K.)

Figure 17 provides further quantitative comparison of the normalized reconstruction error in the reaction rate vector. The normalized reconstruction error ε_S is defined as

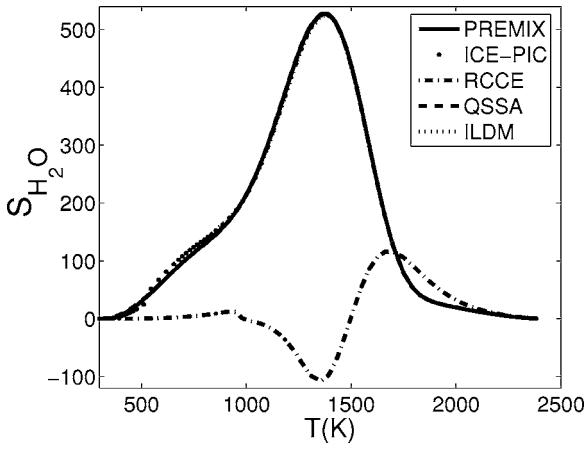

FIG. 16. Reaction rates of H_2O across the flame based on PREMIX calculations and different reconstructed compositions. The profiles are plotted against the temperature $T^P(x)$, which is an increasing function of distance x through the flame.

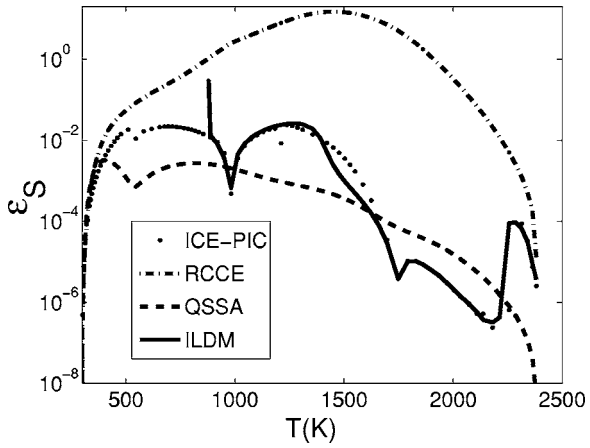

FIG. 17. Normalized errors [Eq. (36)] in the reconstructed reaction rate vectors. The profiles are plotted against the temperature $T^P(x)$, which is an increasing function of distance x through the flame.

$$\varepsilon_S = \frac{|\mathbf{S}(\mathbf{z}^{\mathcal{M}}) - \mathbf{S}(\mathbf{z}^P)|}{S_{\max}}, \tag{36}$$

where $S_{\max}=944$ kmol/(kg s) is the maximum value of $|\mathbf{S}(\mathbf{z}^P)|$ across the flame. From the figure, it is readily observed that RCCE incurs much larger errors than all the other methods with a peak of $\varepsilon_S^{\mathrm{RCCE}}=15$ at $T=1450$ K. In the range $T>875$ K, ICE-PIC, ILDM, and QSSA all yield small errors (less than 0.03), with $\varepsilon_S^{\mathrm{ICE}}$ being very similar to $\varepsilon_S^{\mathrm{ILDM}}$. Notice that there is a steep increase in $\varepsilon_S^{\mathrm{ILDM}}$ around $T=875$ K. Closer examination shows that this occurs just before $\mathbf{z}^{\mathrm{ILDM}}$ becomes unrealizable ($z_{\mathrm{H_2O_2}}^{\mathrm{ILDM}}$ becomes negative, see Fig. 14). Over the entire temperature range, $\varepsilon_S^{\mathrm{ICE}}$ is less than 0.024 and $\varepsilon_S^{\mathrm{QSSA}}$ is less than 3.2×10^{-3}. (Note that this comparison favors QSSA because of the omission of errors in OH and O in QSSA.)

VI. DISCUSSION AND CONCLUSION

The ICE-PIC method presented in this article is a useful tool for simplifying complex chemical kinetics. In numerical simulations of chemically reacting flows, the ICE-PIC method can be used in conjunction with a storage/retrieval method such as ISAT (Ref. 8) to reduce substantially the computational cost of implementing the chemical kinetics.

The ICE-PIC method is based on three major ingredients: the constrained equilibrium manifold the trajectory-generated manifold, and the preimage curve method. The low-dimensional manifold employed in the ICE-PIC method is a trajectory-generated invariant manifold from the constrained equilibrium edge (i.e., it is the time-flow image of the constrained equilibrium edge). This ICE manifold is invariant, continuous, and piecewise smooth. With a reasonable choice of represented species, the manifold is not folded, and hence is given by a graph of a function of the represented variables, i.e., $\mathbf{z}^{\mathrm{ICE}}(\mathbf{z}^e,\mathbf{r})$. The ICE-PIC method employs the constrained equilibrium preimage curve to determine locally the full composition on the ICE manifold. In comparison to other existing dimension-reduction methods such as QSSA, RCCE, and ILDM, this method is the first approach that locally determines compositions on a low-dimensional invariant manifold. Because it is local, the ICE-PIC method can readily be applied to high-dimensional systems. This will be demonstrated in future work.

The method is demonstrated here for the idealized H_2/O system with six chemical species, and it is tested for the premixed laminar flame of a stoichiometric hydrogen/air mixture, where the detailed mechanism with nine species and 21 reactions is employed. With four represented species, H_2, O_2, H_2O, and H, the ICE-PIC method reconstructs the full composition accurately compared with the results obtained by PREMIX with the detailed mechanism. The normalized error ε_z in the composition reconstructed by the ICE-PIC method is less than 3×10^{-4} and the error in the reconstructed temperature is less than 1.5×10^{-3} throughout the flame. Besides the composition, the ICE-PIC method also reproduces the chemical kinetics accurately (see Fig. 17).

Apart from the detailed kinetic mechanism, the only "input" to the ICE-PIC method is the choice of the reduced compositions, e.g., the specification of n_r and of the $n_s\times n_r$ matrix $\mathbf{B}$ (and T_{low} in the adiabatic case). The effect of different choices of reduced representations will be investigated in future work: it is expected that the ICE manifold is weakly dependent on $\mathbf{B}$, away from the realizable boundaries. Another important question to be addressed in future work is to determine the minimum dimension of the ICE manifold required to describe a particular chemical system with prescribed accuracy, i.e., the minimum number of represented variables n_r required. (For other dimension-reduction methods, some studies on the minimum dimensions required have been reported.[13,14,40–42]) Further work includes the application of this method to more complex chemical kinetic systems (such as methane/air and heptane/air systems) and a computationally-efficient implementation of the method combined with ISAT for application to the simulation and modeling of turbulent combustion.

ACKNOWLEDGMENTS

This research is supported by the National Science Foundation through Grant No. CTS-0426787. Helpful comments were received from Stephen Vavasis and Paul Chew. The authors are grateful to Chris Pelkie and Steve Lantz at Cornell Theory Center for help with the graphics.

[1] R. Cao and S. B. Pope, Combust. Flame **143**, 450 (2005).
[2] H. J. Curran, P. Gaffuri, W. J. Pitz, and C. K. Westbrook, Combust. Flame **129**, 253 (2002).
[3] T. Lu and C. K. Law, Proc. Combust. Inst. **30**, 1333 (2005).
[4] P. Pepiot and H. Pitsch, Fourth Joint Meeting of the U.S. Sections of the Combustion Institute, Philadelphia, PA, 21–23 March 2005 (unpublished).
[5] J. F. Griffiths, Prog. Energy Combust. Sci. **21**, 25 (1995).
[6] A. S. Tomlin, T. Turányi, and M. J. Pilling, in *Low-Temperature Combustion and Autoignition*, Comprehensive Chemical Kinetics, Vol. 35 (Elsevier, Amsterdam, 1997).
[7] M. S. Okino and M. L. Mavrovouniotis, Chem. Rev. (Washington, D.C.) **98**, 391 (1998).
[8] S. B. Pope, Combust. Theory Modell. **1**, 41 (1997).
[9] M. Bodenstein and S. C. Lind, Z. Phys. Chem., Stoechiom. Verwandtschaftsl. **57**, 168 (1906).
[10] *Reduced Kinetic Mechanisms and Asymptotic Approximations for Methane-Air Flames*, Lecture Notes in Physics, Vol. 384, edited by M. D. Smooke (Springer, Berlin, 1991).
[11] A. Zagaris, H. G. Kaper, and T. J. Kaper, J. Nonlinear Sci. **14**, 59 (2004).

[12] A. Zagaris, H. G. Kaper, and T. J. Kaper, Multiscale Model. Simul. **2**, 613 (2004).
[13] S. H. Lam and D. A. Goussis, Int. J. Chem. Kinet. **26**, 461 (1994).
[14] Z. Ren and S. B. Pope, Combust. Theory Modell. (to be published).
[15] J. Y. Chen, Combust. Sci. Technol. **57**, 89 (1988).
[16] Z. Ren and S. B. Pope, Combust. Flame **137**, 251 (2004).
[17] J. C. Keck and D. Gillespie, Combust. Flame **17**, 237 (1971).
[18] J. C. Keck, Prog. Energy Combust. Sci. **16**, 125 (1990).
[19] Q. Tang and S. B. Pope, Proc. Combust. Inst. **29**, 1411 (2002).
[20] U. A. Maas and S. B. Pope, Combust. Flame **88**, 239 (1992).
[21] S. B. Pope and U. Maas, Cornell University, Report No. FDA 93-11, 1993 (unpublished).
[22] J. A. van Oijen and L. P. H. de Goey, Combust. Sci. Technol. **161**, 113 (2000).
[23] M. R. Roussel and S. J. Fraser, J. Phys. Chem. **97**, 8316 (1993).
[24] A. N. Gorban and I. V. Karlin, Chem. Eng. Sci. **58**, 4751 (2003).
[25] Z. Ren and S. B. Pope, Proc. Combust. Inst. **30**, 1293 (2005).
[26] M. J. Davis and R. T. Skodje, J. Chem. Phys. **111**, 859 (1999).
[27] R. T. Skodje and M. J. Davis, J. Phys. Chem. A **105**, 10356 (2001).
[28] S. Singh, J. M. Powers, and S. Paolucci, J. Chem. Phys. **117**, 1482 (2002).
[29] J. Li, Z. Zhao, A. Kazakov, and F. L. Dryer, Fall Technical Meeting of the Eastern States Section of the Combustion Institute, Pennsylvania State University, University Park, PA, 26–29 October 2003 (unpublished).
[30] S. B. Pope, Cornell University Report No. FDA 03-02, 2003 (unpublished).
[31] S. B. Pope, Combust. Flame **139**, 222 (2004).
[32] M. Caracotsios and W. E. Stewart, Comput. Chem. Eng. **9**, 359 (1985).
[33] ADIFOR 2.0, Automatic Differentiation of Fortran, http://www-unix.mcs.anl.gov/autodiff/ADIFOR/
[34] W. C. Reynolds, "The Element Potential Method for Chemical Equilibrium Analysis: Implementation in the Interactive Program STANJAN," Technical Report, Mechanical Engineering Department, Stanford University, 1986 (unpublished).
[35] S. Gordon and B. J. McBride, NASA Reference Publication Report No. 1311, 1994 (unpublished).
[36] P. S. Bishnu, D. Hamiroune, M. Metghalchi, and J. C. Keck, Combust. Theory Modell. **1**, 295 (1997).
[37] C. J. Sung, C. K. Law, and J. Y. Chen, Combust. Flame **125**, 906 (2001).
[38] S. B. Pope, Flow, Turbul. Combust. **72**, 219 (2004).
[39] T. Lu, Y. Ju, and C. K. Law, Combust. Flame **126**, 1445 (2001).
[40] S. H. Lam, Combust. Sci. Technol. **89**, 375 (1993).
[41] A. S. Tomlin, L. Whitehouse, R. Lowe, and M. J. Pilling, Faraday Discuss. **120**, 125 (2002).
[42] J. Zobeley, D. Lebiedz, J. Kammerer, A. Ishmurzin, and U. Kummer, in "Transactions on Computational Systems Biology 1", *Lecture Notes in Computer Science 3380* (Springer 2005).